Structure by Architecture: Disentangled Representations without Regularization

Anonymous authors
Paper under double-blind review

Abstract

We study the problem of self-supervised structured representation learning using autoencoders for downstream tasks such as generative modeling. Unlike most methods which rely on matching an arbitrary, relatively unstructured, prior distribution for sampling, we propose a sampling technique that relies solely on the independence of latent variables, thereby avoiding the trade-off between reconstruction quality and generative performance inherent to VAEs. We design a novel autoencoder architecture capable of learning a structured representation without the need for aggressive regularization. Our *structural decoders* learn a hierarchy of latent variables, akin to structural causal models, thereby ordering the information without any additional regularization. We demonstrate how these models learn a representation that improves results in a variety of downstream tasks including generation, disentanglement, and extrapolation using several challenging and natural image datasets.

1 Introduction

Deep learning has achieved strong results on a plethora of challenging tasks. However, performing well on a highly specific dataset is usually insufficient to generalize across real-world problems (Tan et al., 2018; Zhuang et al., 2019). This has led to a particular interest in learning structured representations with useful properties to help with a variety of downstream tasks (Bengio et al., 2013; Tschannen et al., 2018; Bengio et al., 2017; Tschannen et al., 2018; Radhakrishnan et al., 2018). Here, deep learning provides a flexible paradigm to train complex architectures based on autoencoders (Ballard, 1987; Lange & Riedmiller, 2010) which are typically latent variable models, thus allowing us to embed inductive biases into the models to further structure the representations. However, it is still unclear what kinds of structure in a representation are the most effective for generative modeling and how to learn such structures without supervision (Locatello et al., 2018; Khrulkov et al., 2021; Shu et al., 2019; Chen et al., 2020; Nie et al., 2020; Mathieu et al., 2019; Vaswani et al., 2017; Kwon & Ye, 2021). One direction that may contribute to an answer is causal modeling, as it focuses on the underlying (causal) mechanisms that generate the observations, instead of relying on (possibly spurious) correlations (Pearl, 2009; Peters et al., 2017; Louizos et al., 2017; Mitrovic et al., 2020; Shen et al., 2020).

With the versatility of deep learning on one hand, and the conceptual insights of causality on the other, our contributions herein include:

- We propose an architecture called the *Structural Autoencoder* (SAE), where the *structural decoder* emulates a general acyclic structural causal model to learn a hierarchical representation that can separate and order the underlying factors of variation in the data.
- We provide a sampling method, called *hybrid* sampling akin to interventions in the learned SCM which relies only on independence between latent variables, rather than fixing the whole latent distribution.
- We investigate the generalization capabilities of the encoder and decoder separately to better motivate the SAE architecture and to assess how the learned representation of an autoencoder can be adapted to novel factors of variation.

We release our code at `*anonymized*`.

1.1 Related Work

The most popular autoencoder based method is the Variational Autoencoder (VAE) (Kingma & Welling, 2013a), the closely related βVAE (Higgins et al., 2017), and other disentanglement-specific variants like the FactorVAE (Kim & Mnih, 2018) or the β-TCVAE (Chen et al., 2018). These methods focus on matching the latent distribution to a known prior distribution by regularizing the reconstruction training objective (Locatello et al., 2020; Zhou et al., 2020). Although this structure is convenient for generative modeling and even tends to disentangle the latent space to some extent, it comes at the cost of somewhat blurry images due to posterior collapse and holes in the latent space (Locatello et al., 2018; Higgins et al., 2017; Burgess et al., 2018; Kim & Mnih, 2018; Stühmer et al., 2020).

To mitigate the double-edged nature of VAEs, less aggressive regularization techniques have been proposed such as the Wasserstein Autoencoder (WAE), which focuses on the aggregate posterior (Tolstikhin et al., 2018). Unfortunately, WAEs generally fail to produce a particularly meaningful or disentangled latent space (Rubenstein et al., 2018), unless weak supervision is available (Han et al., 2021).

A more structured alternative is the Variational Ladder autoencoder (VLAE) (Zhao et al., 2017) which separates the latent space into separate chunks each of which is processed at different levels of the encoder and decoder (called "rungs"). However, due to the regularization, VLAEs suffer from the same trade-offs as conventional VAEs. Our proposed method makes use of the hierarchical architecture of VLAEs but seeks to improve performance and simplify training by removing the aggressive regularization . In contrast to the ladder rungs, we use Str-Tfm layers (see section 2.2) to infuse information from the latent vector in the decoder irrespective of the encoder architecture. Consequently, unlike VLAEs, SAEs use a conventional feed-forward CNN encoder (like all the other unstructured methods), which improves training stability, simplifies analysis, and underscores the importance of carefully designing the decoder architecture (see further discussion in section 4.2).

2 Methods

2.1 Causal Representation Learning

A *structural causal model (SCM)* represents the relationship between random variables S_i using a directed acyclic graph (DAG) whose edges indicate direct causation and *structural assignments* of the form

$$S_i := f_i(\mathbf{PA}_i, U_i), \qquad (i = 1, \dots, D), \tag{1}$$

encoding the dependence of variable S_i on its parents $\mathbf{PA}_i$ in the graph and on an "unexplained" noise variable U_i (Pearl, 2009). The noises $U_1, \dots, U_D$ are assumed to be jointly independent. Any joint distribution of the S_i can be expressed as an SCM using suitable f_i and U_i. However, the SCM contains additional information regarding how statistical dependencies between the S_i are *generated* by mechanisms (1), such that changes due to *interventions* can be modelled as well (e.g., by setting some U_i to constants).

Real-world observations are often not structured into meaningful causal variables and mechanisms to begin with. E.g., images are high-dimensional, and it is hard to learn objects and their causal relationships from data (Lopez-Paz et al., 2017). One may thus attempt to learn a *representation* consisting of causal variables or disentangled "factors" which are statistically independent (Higgins et al., 2017). However, in an SCM it is not the S_i that should be statistically independent, but the U_i. For this reason, our representations will comprise the U_i as latent variables, driving causal mechanisms via learned functions f_i as described in (1). This embeds an SCM into a larger model whose inputs and outputs may be high-dimensional and unstructured (Schölkopf, 2019), and provides a justification for encouraging statistical independence among the latent variables.

Given (high-dimensional) $X = (X_1, \dots, X_d)$, our goal is to learn a low-dimensional representation $U = (U_1, \dots, U_D)$ $(D \ll d)$ using an **encoder** $\mathbb{R}^d \to \mathbb{R}^D$, and model the generative process (including the SCM) that produced X from the inferred latent variables using a **decoder** $\mathbb{R}^D \to \mathbb{R}^d$. If the causal structure of

the true generative process was known, the topology of the decoder could be fixed accordingly. However, in the fully unsupervised setting, the decoder must be capable of modeling a general SCM, so our architecture specifies a causal ordering (while learning what information to embed in the specified ordering), and the edges between parents and children in the SCM are learned implicitly in the computation layers. Specifically, the learned generative process, a.k.a. decoder, produces a reconstruction $\hat{X}$ of X by feeding each of the U_i into subsequent computation layers. Here, the root node S_1 in the DAG only depends on U_1, while later S_i depend on their noise U_i and potentially their parents $S_j (j < i)$. Thus the depth in the network corresponds to a causal ordering (see appendix for further discussion).

2.2 Structural Decoders

This model architecture is implemented by the *structural decoder*, using D Structural-Transform (Str-Tfm) layers placed evenly in between the convolution blocks. From the corresponding latent variable U_i, the ith Str-Tfm layer estimates a scale α_i and bias β_i which are then used to pixelwise transform the features of the lth layer v_l (as seen in figure 1) much like in Ada-IN (Karras et al., 2019) except without the preceding normalization.

Each Str-Tfm layer thus acts like an f_i in (1) by integrating the information from a latent variable U_i to transform the features $\mathbf{PA}_i$ from earlier layers. This variable decoder depth for each of the latent variables biases high-level non-linear information towards the earlier (and thereby deeper) latent variables, while the model capacity is reduced for the later variables so they can only capture relatively low-level linear features with respect to the data space. Meanwhile, the random initialization of the Str-Tfm layers produce more distinct activations with respect to each of the latent variables than if they were all transformed linearly by the same dense layers. This architectural asymmetry between latent variables thereby encourages statistical independence and induces a relatively intuitive hierarchical structure of the latent space.

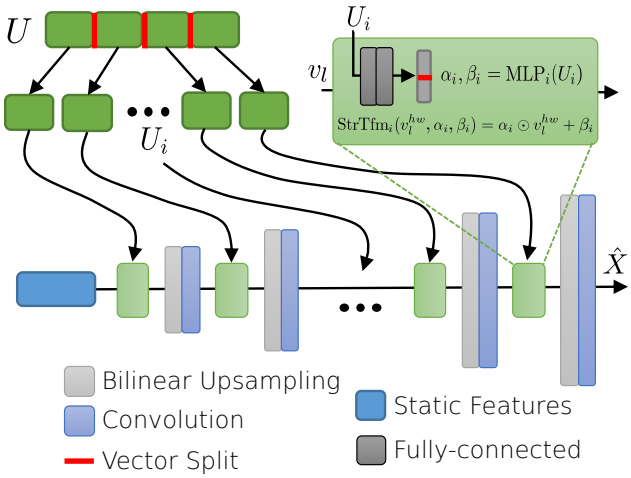

Figure 1: The Structural Decoder reconstructs (or generates) a sample from a latent vector U by first splitting U into D variables each of which transforms the image features after the convolution block l of the model using the corresponding Str-Tfm layer (green box where each pixel v_l^{hw} is transformed by layer specific α_i and β_i which are extracted from the latent variable U_i by network MLP_i).

Although these architectural constraints may help, in theory, without some form of supervision or side information, the learned latent variables are not guaranteed to disentangle the true factors of variation (Locatello et al., 2018), and our learned SCM need not match the true one, thus our algorithm does not constitute an actual causal discovery method Spirtes et al. (2000). Instead, all we are guaranteed from training on observational data is that the model is optimized to reproduce the same observational distribution as the true generative process. Disentanglement methods are commonly evaluated with synthetic datasets where the factors of variation are independent by design (Träuble et al., 2021). For methods penalizing correlations, this implicitly biases the latent variables to align with the true factors. However, the view that disentanglement can be reduced to statistical independence has been contested Träuble et al. (2021); Schölkopf et al. (2021). We treat disentanglement as measured by common metrics not as the objective of our model, but merely as a tool to understand the structure of the representation. Independence of latent variables implies that interventions on them do not violate the learned generative process (i.e., the decoder), thereby enabling hybrid sampling as an alternative to variational regularization techniques for generative modeling.

2.3 Hybrid Sampling

For generative modeling, it is necessary to sample novel latent vectors that are transformed into (synthetic) observations using the decoder. Usually, this is done by regularizing the training objective so the posterior matches some simple prior (e.g. the standard normal). However, in practice, regularization techniques can fail to adequately match the prior and actually exacerbate the information bottleneck, leading to blurry samples from holes in the learned latent distribution and unused latent dimensions due to posterior collapse (Dai & Wipf, 2019; Stühmer et al., 2020; Lucas et al., 2019; Hoffman & Johnson, 2016). Instead of trying to match some prior distribution in the latent space, we suggest an alternative sampling method that eliminates the need for any regularization of the loss. Inspired by Besserve et al. (2018), we refer to it as *hybrid* sampling. The goal is to draw new latent samples $\tilde{U}$ from a distribution having independent variables with marginals matching those observed in the training set, leading to $p(\tilde{U}) \approx \prod_i p(U_i)$. In practice, we first store a set of N ($= 128$ in our case) latent vectors $\{U^{(j)}\}_{j=1}^N$, selected uniformly at random from the training set. We then generate latent samples from $\tilde{U}$ by choosing independently the value for each variable $\tilde{U}_i$, which is sampled uniformly at random from the corresponding set of values of this variable in the stored vectors $\{U_i^{(j)}\}_{j=1}^N$.

This allows the model to generate a diversity of samples well beyond the size of the training set (N^D distinct latent vectors), spanning the Cartesian product of the supports of the (marginal) distribution of each U_i on the training data, which includes the support of the joint latent distribution of U observed during training. Note that hybrid sampling is directly applicable to any learned representation as it does not affect training at all, however the fidelity of generated samples will diminish if there are strong correlations between latent dimensions. Consequently, the goal is to achieve maximal independence between latent variables without compromising on the fidelity of the decoder (i.e., reconstruction error). Not only does this align well with the objectives of unsupervised disentanglement methods, but it is also consistent with the causal perspective of the latent variables as independent noises U_i driving an SCM.

3 Experiments

We train the proposed methods and baselines on two smaller disentanglement datasets (where $d = 64 \times 64 \times 3$ and the true factors are independent): 3D-Shapes (Burgess & Kim, 2018) and the three variants ("toy", "sim", and "real") of the MPI3D Disentanglement dataset (Gondal et al., 2019), as well as two larger more realistic datasets (where $d = 128 \times 128 \times 3$): Celeb-A (Liu et al., 2015) and the Robot Finger Dataset (RFD) (Dittadi et al., 2020).

After training our models on a standard 70-10-20 (train-val-test) split of the datasets we evaluate the quality of the reconstructions based on the reconstruction loss (using binary cross entropy loss, same as the optimization objective) and the Fréchet Inception Distance (FID) (Heusel et al., 2017) as in Williams et al. (2020). The FID is able to capture higher level visual features and can be used to directly compare the reconstructed and generated sample quality, while the binary cross entropy is a purely pixelwise comparison.

Next we compare the performance of the hybrid sampling method to the prior based sampling. Unlike the prior based sampling, which only makes sense for the models that use regularization , the hybrid sampling method can be applied to any latent variable model. Finally we take a closer look at the representations to understand how the model architecture affects the induced structure and disentanglement.

3.1 Models

All models use the same CNN backbone for both the encoder and decoder with the same number of convolution blocks (see the appendix for details). For the smaller datasets, the encoder and decoder have 12 convolution blocks, the latent space has 12 dimensions in total, and the models are trained for 100k iterations, while for CelebA and RFD each the encoder/decoder has 16 convolution blocks each with twice as many filters, the latent space is 32 dimensional in total, and the models are trained for 200k iterations.

We compare four kinds of autoencoder architectures. The first type is our Structural Autoencoders (SAE) which use a conventional encoder and a structural decoder with the latent space split evenly into 2, 3, 4, 6, or 12 variables for the smaller datasets and 16 variables for the larger ones corresponding to the

labels SAE-2, SAE-3, SAE-4, SAE-6, SAE-12 and SAE-16 respectively. Consequently, the "structural" architecture has an architectural asymmetry between latent variables in the decoder, but not in the encoder. The simplest "baseline" architecture uses the traditional "hourglass" architecture, in addition to a variety of different regularization methods: (1) unregularized autoencoders ("AE"), (2) Wasserstein-autoencoders ("WAE") (Tolstikhin et al., 2018), (3) VAE (Kingma & Welling, 2013b), (4) βVAE (Higgins et al., 2017), (5) FactorVAE ("FVAE") (Kim & Mnih, 2018), and (6) β-TCVAE (using the experimentally determined best hyperparameters, see the appendix A.2.2). The next baseline architecture is called "AdaAE" (and referred to as "Adaptive"). It is identical to the SAE models except that all latent variables are passed to each of the Str-Tfm layers, so the architecture has connections between the latent variables and intermediate layers, but without the architectural asymmetry. For the purposes of hybrid sampling, each latent dimension of these less structured baselines is treated as a separate latent variable. The final type of architecture we investigate is the Variational Ladder Autoencoder (Zhao et al., 2017) which also learns a hierarchical representation, but unlike the Structural Autoencoders, VLAEs also use the variational regularization and use an encoder architecture that roughly mirrors the decoder, consequently both the encoder and decoder break the architectural symmetry between latent variables. Just like for the SAEs, we include variants of the VLAEs with 2, 3, 4, 6, 12, and 16 rungs.

3.2 Extrapolation

Since VLAEs structure both the encoder and decoder, while SAEs only structure the decoder, we aim to better characterize the relative behaviors of the encoder and decoder. Specifically, this analysis aims to understand to what extent the encoder or decoder is the "weaker link" in regards to integrating new information into the representation.

First, both the encoder and decoder are trained jointly on a subset of 3D-Shapes where only three distinct shapes exist (instead of four, as the ball is missing) for 80k iterations. Then either the encoder only, the decoder only, or both are trained for another 20k iterations on the full 3D-Shapes training dataset. The reconstruction error for samples not seen during any part of training is compared for each of the variants and each of the architectures to identify how well the encoder extrapolates compared to the decoder, and to assay implications for designing novel autoencoder architectures.

4 Results

In terms of reconstruction quality, the structural autoencoder architecture consistently outperforms the baselines (figure 2). As expected, unregularized methods like the SAE, AdaAE, and AE tend to have significantly better reconstruction quality. However, also noteworthy is that the structured architectures SAE and VLAE show improved results compared to their unstructured counterparts. It should be noted that there is some controversy regarding the reliability of FID with synthetic datasets (Razavi et al., 2019; Barratt & Sharma, 2018). However, we consistently find strong agreement between the reconstruction FID and the pixelwise metrics (see figure 8 in the appendix for further discussion).

Comparing the SAE models to the AdaAE architecture, we see that there can be a slight penalty in reconstruction quality incurred from separately processing the latent variables. However, this is more than made up for in the quality of the generated samples (shown in figure 3), where the SAE models perform significantly better than the baselines. Even the regularized models such as VLAE, FVAEs, and VAEs consistently generate higher quality samples using the hybrid sampling than when sampling from the prior they were trained to match (also in figure 6b). Surprisingly, the AdaAE architecture actually outperforms all other models on CelebA using hybrid sampling. This may be explained by the severity of the information bottleneck experienced when embedding CelebA into only 32 dimensions. Consequently, the higher fidelity decoder from the intermediate connections of the latent vector exceed the performance penalty incurred by the hybrid sampling when disregarding the correlations between latent variables.

In general, if we consider the latent distribution , then sampling from the approximated factorized prior can introduce at least two types of errors: (1) errors due to not taking into account statistical dependences among latent variables, and (2) errors due to sampling from "holes" in the latent distribution if the prior

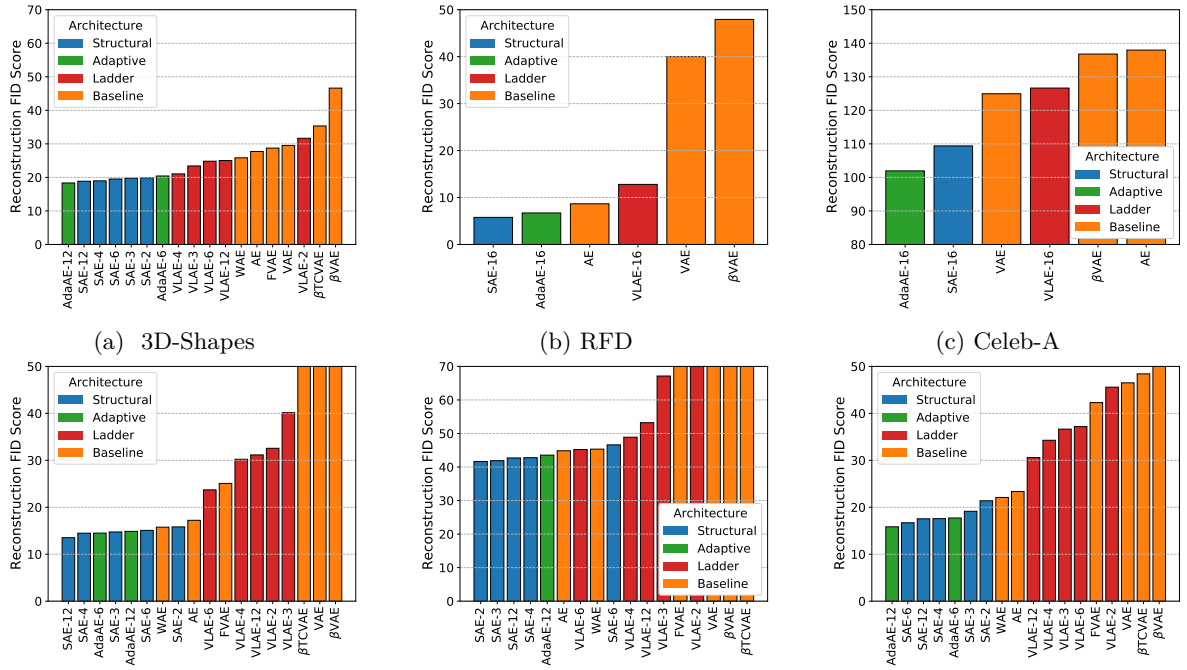

(a) 3D-Shapes (b) RFD (c) Celeb-A

(d) MPI3D Toy (e) MPI3D Sim (f) MPI3D Real

Figure 2: Reconstruction quality for all models and datasets. "Baseline" models correspond to traditional "hourglass" CNN architectures, while the "Structural" models use our novel architectures to further structure the learned representation.

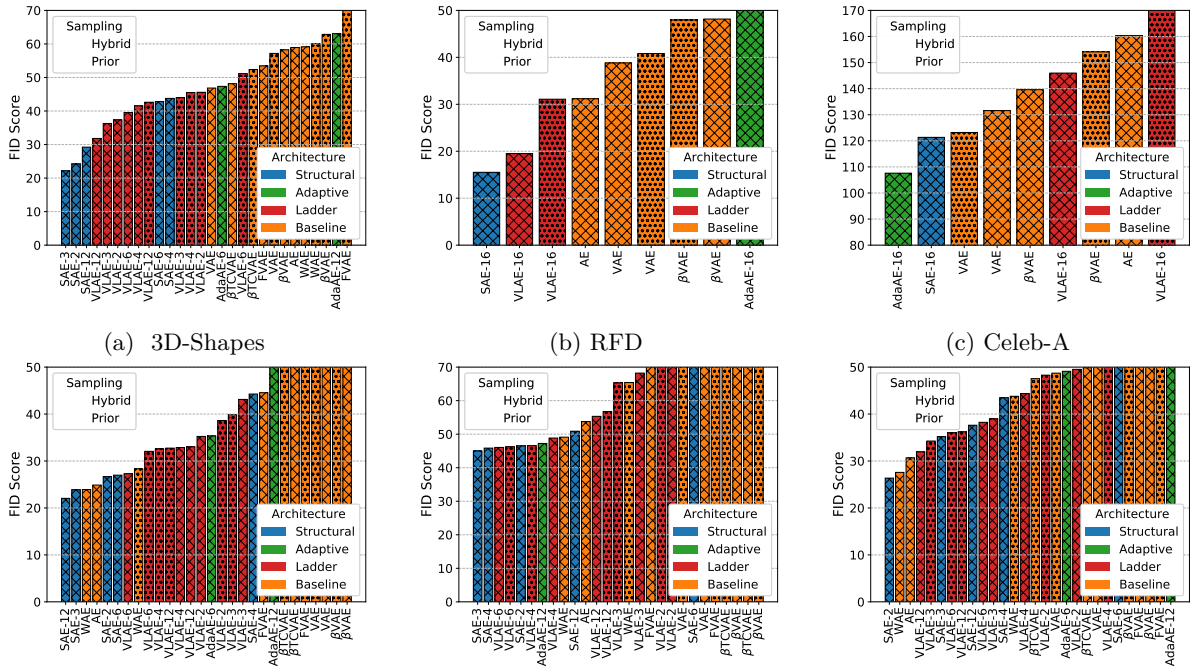

(a) 3D-Shapes (b) RFD (c) Celeb-A

(d) MPI3D Toy (e) MPI3D Sim (f) MPI3D Real

Figure 3: Quality of the generated samples using different models and sampling methods. Note that our SAE models perform well without having to regularize the latent space towards a prior. In fact, even with the conventional "hourglass" architecture (in orange), the hybrid sampling method generates relatively high quality samples, often outperforming the prior-based sampling.

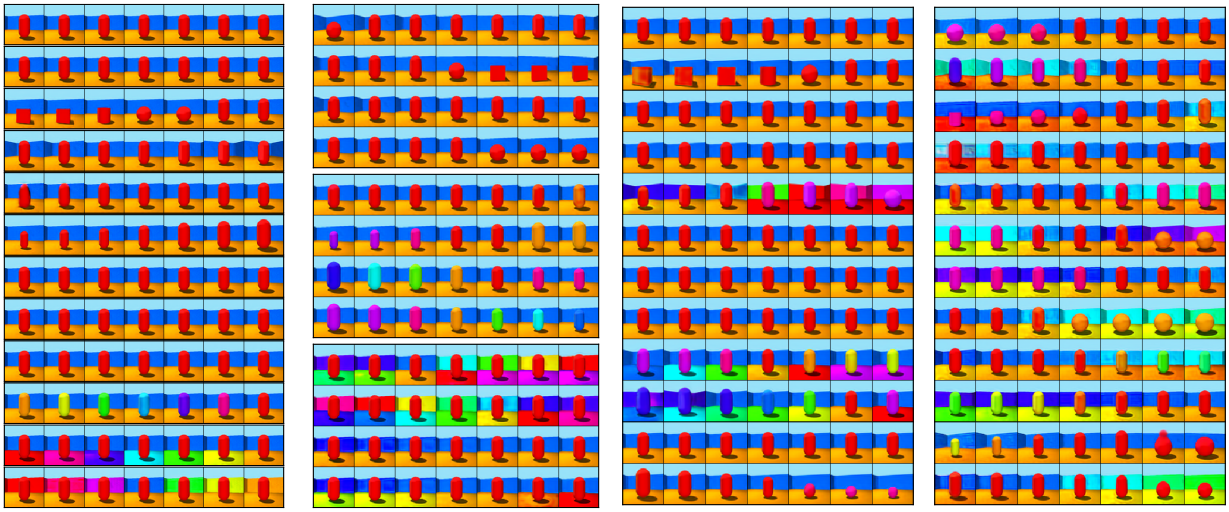

(a) SAE-12 (b) SAE-3 (c) VAE (d) AdaAE-12

Figure 4: Latent traversals of several models trained on 3D-Shapes, in the original order. Note the ordering of the information in the structural decoder models (SAE-12 and SAE-3) where higher level, nonlinear features (like shape and orientation) are encoded in the first few dimensions, which are located deeper in the network.

Model	DCI	MIG	IRS	Mod	Exp
SAE-12	**0.974**	0.537	**0.830**	**0.967**	**1.000**
SAE-6	0.865	0.225	0.735	0.966	0.999
SAE-4	0.740	0.209	0.654	0.945	0.999
VLAE-12	0.832	**0.553**	0.751	0.914	0.977
VLAE-6	0.785	0.326	0.689	0.929	0.963
VLAE-4	0.690	0.282	0.544	0.900	0.926
βTCVAE	0.410	0.237	0.603	0.865	0.923
FVAE	0.330	0.123	0.725	0.907	0.955
βVAE	0.235	0.127	0.593	0.879	0.799
VAE	0.314	0.138	0.607	0.892	0.872
WAE	0.211	0.050	0.621	0.946	0.906
AE	0.307	0.092	0.638	0.926	0.943
AdaAE-12	0.299	0.062	0.503	0.876	0.999

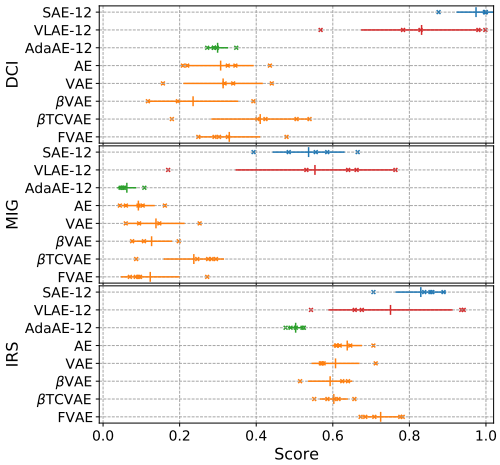

Figure 5: Disentanglement scores for 3D-Shapes. DCI denotes the DCI disentanglement score (Eastwood & Williams, 2018), MIG is the Mutual Information Gap (Chen et al., 2018), IRS is the Interventional Robustness Score (Suter et al., 2018), and Mod/Exp refers to the Modularity/Explicitness scores respectively (Ridgeway & Mozer, 2018) (for all these metrics higher is better). The figure on the right shows how the scores vary across five models with different random seeds marked with a cross (lines indicate the resulting mean and standard deviation). Both hierarchical methods, SAE-12 and the VLAE-12, outperform all other baselines, and in particular the SAE performs well, despite the lack of regularization.

does not match it everywhere. Whenever (2) is the dominating source of error, hybrid sampling is preferred. Furthermore, learning independent latent variables aligns with the aim towards disentangled representations, while minimizing the divergence between the posterior and prior results in a compromise that does not necessarily promote disentanglement.

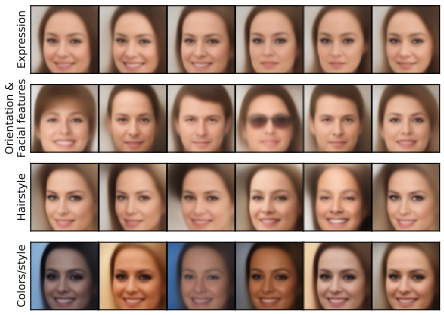

(a) Here we use hybridized chunks of latent vector to show how different aspects of the resulting generated image can be affected using our SAE-16 architecture and hybrid sampling technique. For each row the corresponding quarter of latent dimensions (8/32) are hybridized (see section 2.3) while the remaining 3/4 dimensions are fixed. This shows how the SAE architecture is able to order partially disentangled factors of variation from high-level (more nonlinear, like facial expressions and features) to low-level (such as color/lighting) without any additional regularization or supervision.

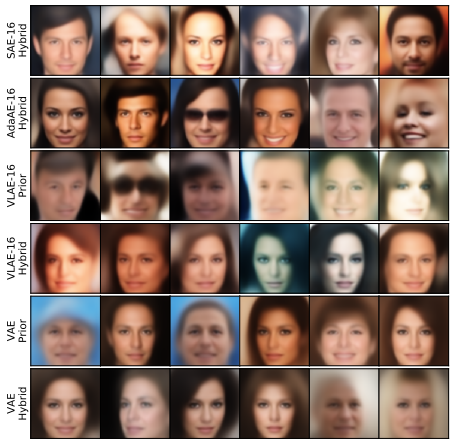

(b) Samples generated using hybrid and prior-based sampling using several models trained on CelebA. Note that the hybrid sampling tends to produce relatively high quality samples both for our proposed SAE and AdaAE architectures as well as baselines.

Figure 6: CelebA Controllable Generation and Sampling Comparison

4.1 Hierarchical Structure

To get a rough idea of how the representations learned using the structural decoders differ from more conventional architectures, figure 4 shows the one dimensional latent traversals (i.e., each row corresponds to the decoder outputs when incrementally increasing the corresponding latent dimension at a time from the min to the max value observed). The traversals illustrate the hierarchical structure in the representation learned by the SAE models: the information encoded in the first few latent variables can be more nonlinear with respect to the output (pixel) space, as the decoder has more layers to process that information, while the more linear information must be embedded in the last few variables. This results in a reliable ordering of "high-level" information (such as object shape or camera orientation) first, followed by the "low-level" information (such as color). This means the structural decoder architecture biases the representation to separate and order the information necessary for reconstruction (and generation) in a meaningful way, and thereby ordering, and potentially even fully disentangling, the underlying factors of variation better.

Figure 5 evaluates how disentangled the representations are, using common metrics. The table shows the disentanglement scores of the same models discussed above, while the plot on the right sheds light on quality of the representations varies for five different random seeds (used to initialize the network parameters). Most noteworthy is that the SAE-12 model consistently achieves very high disentanglement scores. This shows, empirically, that the SAE architecture promotes independence between latent variables (especially SAE-12). We may explain this as a consequence of splitting up the latent dimensions so that each variable has a unique parameterization in the decoder, making different latent variables less likely to be processed in the same way.

Unsurprisingly, when there are multiple latent dimensions per variable (like in SAE-6, SAE-4, etc.), the dimensions within a variable are entangled similarly to the baselines like AE or adaptive baselines. Since all of these disentanglment metrics are computed on a dimension-by-dimension basis, the resulting scores are systematically underestimated. Qualitatively, these SAE models still achieve the same ordering of causal mechanisms, as can be seen from figure 4b.

For a real world demonstration of how well SAE models are able to order information in the latent space, figure 6a shows generated CelebA samples when varying only a quarter of the latent variables at a time, with the labels on the left describing roughly the semantic semantic information contained. Note that the

inductive biases are not strong enough to fully disentangle the factors of variation into individual latent dimensions. However, the hierarchical structure learns a diffuse kind of disentanglement where information pertaining to higher-level features tend to be encoded in the first few dimensions while lower level factors of variation show up towards the last few dimensions.

SAE models achieve this structured disentanglement using the Str-Tfm layers as opposed to the standard Ada-In layers. Each Str-Tfm layer only has access to one of the latent variables which is not directly seen by any other part of the decoder. In contrast, the Ada-In layers used by the AdaAE allows information from anywhere in the latent vector to leak into any part of the decoder. Consequently, the AdaAE does not disentangle the representation at all, as seen in the table of figure 5 (although it achieves impressive results for reconstruction nonetheless, see figure 2).

4.2 Extrapolation

Results of the experiment described in section 3.2 are shown on figure 7. Perhaps unsurprisingly, none of the models were particularly adept at zero-shot extrapolation to observations that were not in the initial training data, as is consistent with Schott et al. (2021). Comparing the first two columns on the right , without any update, the reconstructed images filter out the novel information in the sample (in this case, ball shape), and instead reconstruct a similar sample seen during training (a cylinder).

If only the encoder is updated on some observations with the additional shape while the decoder is frozen, then the reconstruction performance increases somewhat, but some deformations and artifacts become visible in the reconstruction. This suggests the frozen decoder struggles to adequately extrapolate, even when the encoder extends the representation to include the ball.

In contrast, when only the decoder is updated, the reconstructions qualitatively look much more similar to the original observations. Although the encoder can be expected to generally filter out any information it has not been trained to encode into the latent space due to the bottleneck, the representation may still extrapolate somewhat provided the decoder can reconstruct any novel features. This underscores the importance of focusing on carefully designing and training the decoder, as embodied by the SAEs, because the decoder is not able to extrapolate as well as the encoder.

Model	Neither	Encoder	Decoder	Both
SAE-12	13.21	7.7	0.42	**0.34**
SAE-6	13.35	7.99	0.52	0.36
VLAE-12	18.37	7.69	1.55	0.62
VAE	12.97	8.78	0.44	0.46
βVAE	15.49	8.31	1.35	0.52
AE	11.81	**7.31**	0.38	0.35
WAE	**11.68**	7.87	**0.37**	0.35

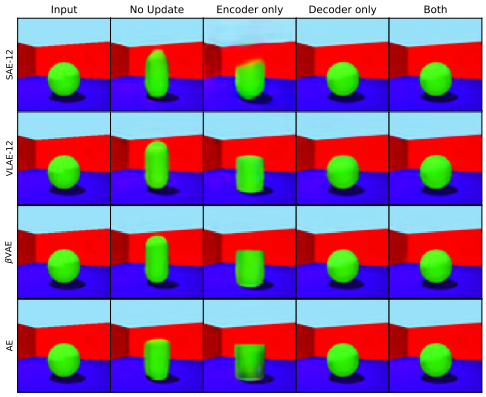

Figure 7: Average reconstruction error (MSE x1000) on novel observations when training either the encoder, decoder, both, or neither on the initially left-out ball shape (see section 3.2). Example input and reconstructed images are shown above. All models perform significantly better when updating the decoder than the encoder, and reach a reconstruction quality that is almost indistinguishable from the model when updating both the encoder and decoder. Furthermore, the SAE-12 generally outperforms all variational baselines, suggesting the aggressive regularization of VAEs makes updating the representation more difficult.

5 Conclusion

While VAEs provide a principled approach to generative modeling with autoencoders, in practice, the regularization tends to suppress the dependence of the posterior on the observations by minimizing its discrepancy

to the prior (Hoffman & Johnson, 2016; Tolstikhin et al., 2018), resulting in a trade-off between reconstruction quality and matching the prior. While regularization may help with disentanglement, this tends to have negative effects on sample quality.

This motivated us to look for an alternate sampling method that does not require aggressive regularization as VAEs. Our hybrid sampling technique relies on a factorized support instead of expecting the learned posterior to match some unstructured prior. This effectively unifies the goals of achieving a disentangled and samplable representation, thereby enabling challenging downstream tasks such as controllable generation.

To exploit the benefits of this sampling, we propose the structural autoencoder architecture inspired by structural causal models, which orders information in the latent space, while also, as shown by our experiments, encouraging independence. Using a pure reconstruction loss, the SAE architecture produces high quality reconstructions and generated samples, improving extrapolation compared to variational baselines as well as achieving a significant degree of disentanglement across a variety of datasets.

While it is encouraging how far one can get with suitable architectural biases, future work should assay whether the learned models can be structured further by more explicit forms of causal training. For instance, we could explicitly encourage the realism of hybrid samples, or the sparsity of latent factor changes across domain shifts based on the Sparse Mechanism Shift Hypothesis (Schölkopf et al., 2021).

References

Dana H Ballard. Modular learning in neural networks. In *AAAI*, pp. 279–284, 1987.

Shane Barratt and Rishi Sharma. A note on the inception score. *arXiv preprint arXiv:1801.01973*, 2018.

Emmanuel Bengio, Valentin Thomas, Joelle Pineau, Doina Precup, and Yoshua Bengio. Independently controllable features, 2017. URL `arXiv:1703.07718`.

Yoshua Bengio, Aaron Courville, and Pascal Vincent. Representation learning: A review and new perspectives. *IEEE transactions on pattern analysis and machine intelligence*, 35(8):1798–1828, 2013.

Michel Besserve, Arash Mehrjou, Rémy Sun, and Bernhard Schölkopf. Counterfactuals uncover the modular structure of deep generative models. *arXiv preprint arXiv:1812.03253*, 2018.

Chris Burgess and Hyunjik Kim. 3d shapes dataset, 2018.

Christopher P Burgess, Irina Higgins, Arka Pal, Loic Matthey, Nick Watters, Guillaume Desjardins, and Alexander Lerchner. Understanding disentangling in β-VAE. *arXiv preprint arXiv:1804.03599*, 2018.

Ricky TQ Chen, Xuechen Li, Roger Grosse, and David Duvenaud. Isolating sources of disentanglement in variational autoencoders. *arXiv preprint arXiv:1802.04942*, 2018.

Shang-Fu Chen, Jia-Wei Yan, Ya-Fan Su, and Yu-Chiang Frank Wang. Deep representation decomposition for feature disentanglement. *arXiv preprint arXiv:2011.00788*, 2020.

Bin Dai and David Wipf. Diagnosing and enhancing VAE models. *arXiv preprint arXiv:1903.05789*, 2019.

Andrea Dittadi, Frederik Träuble, Francesco Locatello, Manuel Wüthrich, Vaibhav Agrawal, Ole Winther, Stefan Bauer, and Bernhard Schölkopf. On the transfer of disentangled representations in realistic settings. *arXiv preprint arXiv:2010.14407*, 2020.

Cian Eastwood and Christopher KI Williams. A framework for the quantitative evaluation of disentangled representations. 2018.

Muhammad Waleed Gondal, Manuel Wüthrich, Djorđe Miladinović, Francesco Locatello, Martin Breidt, Valentin Volchkov, Joel Akpo, Olivier Bachem, Bernhard Schölkopf, and Stefan Bauer. On the transfer of inductive bias from simulation to the real world: a new disentanglement dataset. *arXiv preprint arXiv:1906.03292*, 2019.

Jun Han, Martin Renqiang Min, Ligong Han, Li Erran Li, and Xuan Zhang. Disentangled recurrent Wasserstein autoencoder. *arXiv preprint arXiv:2101.07496*, 2021.

Martin Heusel, Hubert Ramsauer, Thomas Unterthiner, Bernhard Nessler, and Sepp Hochreiter. GANs trained by a two time-scale update rule converge to a local Nash equilibrium. In *Advances in neural information processing systems*, 2017.

Irina Higgins, Loic Matthey, Arka Pal, Christopher Burgess, Xavier Glorot, Matthew Botvinick, Shakir Mohamed, and Alexander Lerchner. beta-VAE: Learning basic visual concepts with a constrained variational framework. *ICLR*, 2(5):6, 2017. URL `https://pdfs.semanticscholar.org/a902/26c41b79f8b06007609f39f82757073641e2.pdf`.

Matthew D Hoffman and Matthew J Johnson. ELBO surgery: yet another way to carve up the variational evidence lower bound. In *Workshop in Advances in Approximate Bayesian Inference, NIPS*, volume 1, pp. 2, 2016.

Tero Karras, Samuli Laine, and Timo Aila. A style-based generator architecture for generative adversarial networks. In *Proceedings of the IEEE Conference on Computer Vision and Pattern Recognition*, 2019. URL `http://openaccess.thecvf.com/content_CVPR_2019/papers/Karras_A_Style-Based_Generator_Architecture_for_Generative_Adversarial_Networks_CVPR_2019_paper.pdf`.

Valentin Khrulkov, Leyla Mirvakhabova, Ivan Oseledets, and Artem Babenko. Disentangled representations from non-disentangled models. *arXiv preprint arXiv:2102.06204*, 2021.

Hyunjik Kim and Andriy Mnih. Disentangling by factorising. *arXiv preprint arXiv:1802.05983*, 2018. URL `https://arxiv.org/pdf/1802.05983.pdf`.

Diederik P. Kingma and Max Welling. Auto-encoding variational Bayes, 2013a. URL `arXiv:1312.6114`.

Diederik P Kingma and Max Welling. Auto-encoding variational bayes. *arXiv preprint arXiv:1312.6114*, 2013b.

Gihyun Kwon and Jong Chul Ye. Diagonal attention and style-based GAN for content-style disentanglement in image generation and translation. *arXiv preprint arXiv:2103.16146*, 2021.

Sascha Lange and Martin Riedmiller. Deep auto-encoder neural networks in reinforcement learning. In *The 2010 International Joint Conference on Neural Networks (IJCNN)*, pp. 1–8. IEEE, 2010.

Ziwei Liu, Ping Luo, Xiaogang Wang, and Xiaoou Tang. Deep learning face attributes in the wild. In *Proceedings of International Conference on Computer Vision (ICCV)*, December 2015.

Francesco Locatello, Stefan Bauer, Mario Lucic, Gunnar Rätsch, Sylvain Gelly, Bernhard Schölkopf, and Olivier Bachem. Challenging common assumptions in the unsupervised learning of disentangled representations. *arXiv preprint arXiv:1811.12359*, 2018.

Francesco Locatello, Stefan Bauer, Mario Lucic, Gunnar Rätsch, Sylvain Gelly, Bernhard Schölkopf, and Olivier Bachem. A sober look at the unsupervised learning of disentangled representations and their evaluation. *Journal of Machine Learning Research (JMLR)*, 2020.

D. Lopez-Paz, R. Nishihara, S. Chintala, B. Schölkopf, and L. Bottou. Discovering causal signals in images. In *IEEE Conference on Computer Vision and Pattern Recognition (CVPR)*, pp. 58–66, 2017.

Christos Louizos, Uri Shalit, Joris Mooij, David Sontag, Richard Zemel, and Max Welling. Causal effect inference with deep latent-variable models. *arXiv preprint arXiv:1705.08821*, 2017.

James Lucas, George Tucker, Roger Grosse, and Mohammad Norouzi. Understanding posterior collapse in generative latent variable models. 2019.

Emile Mathieu, Tom Rainforth, Nana Siddharth, and Yee Whye Teh. Disentangling disentanglement in variational autoencoders. In *International Conference on Machine Learning*, pp. 4402–4412. PMLR, 2019.

Diganta Misra. Mish: A self regularized non-monotonic neural activation function. *arXiv preprint arXiv:1908.08681*, 4, 2019.

Jovana Mitrovic, Brian McWilliams, Jacob Walker, Lars Buesing, and Charles Blundell. Representation learning via invariant causal mechanisms. *arXiv preprint arXiv:2010.07922*, 2020.

Weili Nie, Tero Karras, Animesh Garg, Shoubhik Debnath, Anjul Patney, Ankit Patel, and Animashree Anandkumar. Semi-supervised stylegan for disentanglement learning. In *International Conference on Machine Learning*, pp. 7360–7369. PMLR, 2020.

Adam Paszke, Sam Gross, Francisco Massa, Adam Lerer, James Bradbury, Gregory Chanan, Trevor Killeen, Zeming Lin, Natalia Gimelshein, Luca Antiga, Alban Desmaison, Andreas Kopf, Edward Yang, Zachary DeVito, Martin Raison, Alykhan Tejani, Sasank Chilamkurthy, Benoit Steiner, Lu Fang, Junjie Bai, and Soumith Chintala. PyTorch: An imperative style, high-performance deep learning library. In H. Wallach, H. Larochelle, A. Beygelzimer, F. d'Alché-Buc, E. Fox, and R. Garnett (eds.), *Advances in Neural Information Processing Systems 32*, pp. 8024–8035. Curran Associates, Inc., 2019.

J. Pearl. *Causality: Models, Reasoning, and Inference.* Cambridge University Press, New York, NY, 2nd edition, 2009.

J. Peters, D. Janzing, and B. Schölkopf. *Elements of Causal Inference - Foundations and Learning Algorithms.* MIT Press, Cambridge, MA, USA, 2017.

Adityanarayanan Radhakrishnan, Karren Yang, Mikhail Belkin, and Caroline Uhler. Memorization in overparameterized autoencoders. *arXiv preprint arXiv:1810.10333*, 2018.

Ali Razavi, Aaron van den Oord, and Oriol Vinyals. Generating diverse high-fidelity images with vq-vae-2. In *Advances in neural information processing systems*, pp. 14866–14876, 2019.

Karl Ridgeway and Michael C Mozer. Learning deep disentangled embeddings with the f-statistic loss. *arXiv preprint arXiv:1802.05312*, 2018.

Paul K Rubenstein, Bernhard Schoelkopf, and Ilya Tolstikhin. On the latent space of Wasserstein auto-encoders. *arXiv preprint arXiv:1802.03761*, 2018.

B. Schölkopf. Causality for machine learning, 2019. arXiv:1911.10500.

Bernhard Schölkopf, Francesco Locatello, Stefan Bauer, Nan Rosemary Ke, Nal Kalchbrenner, Anirudh Goyal, and Yoshua Bengio. Toward causal representation learning. *Proceedings of the IEEE*, 109(5): 612–634, 2021.

Lukas Schott, Julius von Kügelgen, Frederik Träuble, Peter Gehler, Chris Russell, Matthias Bethge, Bernhard Schölkopf, Francesco Locatello, and Wieland Brendel. Visual representation learning does not generalize strongly within the same domain. *arXiv preprint arXiv:2107.08221*, 2021.

Xinwei Shen, Furui Liu, Hanze Dong, Qing Lian, Zhitang Chen, and Tong Zhang. Disentangled generative causal representation learning. *arXiv preprint arXiv:2010.02637*, 2020.

Rui Shu, Yining Chen, Abhishek Kumar, Stefano Ermon, and Ben Poole. Weakly supervised disentanglement with guarantees. *arXiv preprint arXiv:1910.09772*, 2019.

Peter Spirtes, Clark N Glymour, Richard Scheines, and David Heckerman. *Causation, prediction, and search.* MIT press, 2000.

Jan Stühmer, Richard Turner, and Sebastian Nowozin. Independent subspace analysis for unsupervised learning of disentangled representations. In *International Conference on Artificial Intelligence and Statistics*, pp. 1200–1210. PMLR, 2020.

Raphael Suter, Dorde Miladinovic, Stefan Bauer, and Bernhard Schölkopf. Interventional robustness of deep latent variable models, 2018. https://arxiv.org/abs/1811.00007v1.

Chuanqi Tan, Fuchun Sun, Tao Kong, Wenchang Zhang, Chao Yang, and Chunfang Liu. A survey on deep transfer learning. In *International conference on artificial neural networks*, pp. 270–279. Springer, 2018.

I. Tolstikhin, O. Bousquet, S. Gelly, and B. Schölkopf. Wasserstein auto-encoders. In *6th International Conference on Learning Representations (ICLR)*, May 2018. URL `https://openreview.net/forum?id=HkL7n1-0b`.

Frederik Träuble, Elliot Creager, Niki Kilbertus, Francesco Locatello, Andrea Dittadi, Anirudh Goyal, Bernhard Schölkopf, and Stefan Bauer. On disentangled representations learned from correlated data. In *International Conference on Machine Learning*, pp. 10401–10412. PMLR, 2021.

Michael Tschannen, Olivier Bachem, and Mario Lucic. Recent advances in autoencoder-based representation learning. *arXiv preprint arXiv:1812.05069*, 2018.

Ashish Vaswani, Noam Shazeer, Niki Parmar, Jakob Uszkoreit, Llion Jones, Aidan N Gomez, Łukasz Kaiser, and Illia Polosukhin. Attention is all you need. In *Advances in neural information processing systems*, pp. 5998–6008, 2017.

Will Williams, Sam Ringer, Tom Ash, John Hughes, David MacLeod, and Jamie Dougherty. Hierarchical quantized autoencoders. *arXiv preprint arXiv:2002.08111*, 2020.

Shengjia Zhao, Jiaming Song, and Stefano Ermon. Learning hierarchical features from deep generative models. In *Proceedings of the 34th International Conference on Machine Learning-Volume 70*, pp. 4091–4099. JMLR.org, 2017.

Sharon Zhou, Eric Zelikman, Fred Lu, Andrew Y Ng, and Stefano Ermon. Evaluating the disentanglement of deep generative models through manifold topology. *arXiv preprint arXiv:2006.03680*, 2020.

Fuzhen Zhuang, Zhiyuan Qi, Keyu Duan, Dongbo Xi, Yongchun Zhu, Hengshu Zhu, Hui Xiong, and Qing He. A comprehensive survey on transfer learning. *arXiv preprint arXiv:1911.02685*, 2019.

A Appendix

A.1 Causal ordering

Suppose we are given (high-dimensional) $X = (X_1, \ldots, X_d)$ (think of X as an image with pixels $X_1, \ldots, X_d$), from which we should construct $S_1, \ldots, S_D$ ($D \ll d$) as well as causal mechanisms

$$S_i := f_i(\mathbf{PA}_i, U_i), \quad (i = 1, \ldots, D). \tag{2}$$

To this end, we first use an **encoder** $f_{enc} : \mathbb{R}^d \to \mathbb{R}^D$ taking X to a latent bottleneck representation comprising $U = (U_1, \ldots, U_D)$. The next step is a map $f(U)$ implementing the structural assignments $f_1, \ldots, f_D$ as a function of U. We construct it as follows: we evaluate the f_i of a root node i, i.e., f_i depends only on U_i. In the step, we evaluate any node j which depends only on its U_j and possibly other variables that have already been computed. We iterate until there are no nodes left. This terminates (since the graph is acyclic) and yields a unique $f(U)$, but the order $\pi(i)$ in which the f_i get evaluated need not be unique. It is referred to as a *causal* or *topological* ordering (Peters et al., 2017), satisfying $\pi(i) < \pi(j)$ whenever j is a descendant of i. This embeds the **SCM** into the network starting from the bottleneck $U = (U_1, \ldots, U_D)$ with the U_i feeding into subsequent computation layers according to a causal ordering. This structure reflects the fact that the root node(s) in the DAG only depend on "their" noise variables, while later ones depend on their noise and those of their parents, and so on. Finally, we apply a **decoder** $f_{dec} : \mathbb{R}^D \to \mathbb{R}^d$. The system can be trained using reconstruction error to satisfy $f_{dec} \circ f \circ f_{enc} \approx id$ on the observed images.

Recall that for a *causally sufficient* system, the set of noises $U_1, \ldots, U_n$ are assumed to be jointly independent. If, in contrast, only a subset of the causal variables are modelled, then the noises will in the generic case be dependent. We would expect that the architectural bias implemented by the structural decoder, however, may still be a sensible one.

A.2 Training Procedure

A.2.1 Architecture Details

As described in the main paper, the basic convolutional backbone of all models is the same. For the smaller datasets, 3D-Shapes and the MPI3D datasets (where observations are 64x64 pixels), the encoder and decoder each have 12 convolutional blocks. Each block has a convolutional layer with 64 channels and a kernel size of 3x3 and stride of 1 (unless otherwise specified), followed by a group normalization layer and then a MISH nonlinearity (Misra, 2019). In the encoder, the features are downsampled using a 2x2 Max Pooling layer right after the convolution every third layer starting with the first one and the first convolution layer uses a kernel size of 5x5. In the decoder, every third convolution layer is immediately preceded by a 2x2 bilinear upsampling. For our structured modules (SAE and AdaAE), the specified number of Str-Tfm layers are placed evenly in between the convolution blocks. For SAE models, the latent space is always split evenly between Str-Tfm layers, and each layer uses a three hidden layer network to process the latent space segment into the scale and bias vectors which are then applied to all pixels individually of the features. For the VLAE models, the inference and generative ladder rungs each also have a three hidden layers to process the features into and out of the separate latent space segments respectively.

While the latent space was always 12 dimensional for 3D-Shapes and MPI3D, for Celeb-A we use a 32 dimensional latent space. For Celeb-A, we also expand the 12 block backbone to 16 blocks and double the filters per convolution layer to 128. The exact sizes and connectivity of the models can be seen in the configuration files of a the attached code, but overall, each of the 3D-Shapes and MPI3D models have approximately 1-1.2M trainable parameters, while for CelebA the models have 6-7M parameters.

A.2.2 Training Details

All models used the same training hyperparameters, which included using an Adam optimizer with a learning rate of 0.0005 and momentum parameters of $\beta_1 = 0.9$ and $\beta_2 = 0.999$. For the smaller datasets (3D-Shapes, MPI3D) the models were trained for 100k iterations and a batch size of 128, while for Celeb-A and RFD the models were trained for 200k iterations and a batch size of 32. The hyperparameters for the RFD dataset

the same as for Celeb-A, except that the number of channels per convolution layer was doubled and the learning rate was decreased by a factor of 10.

The models are implemented using Pytorch (Paszke et al., 2019) and were trained on the in-house computing cluster using Nvidia V100 32GB GPUs, so that training a single model takes about 3-4 hours on the smaller datasets and 7-10 hours for CelebA.

For the β-VAEs and β-TCVAEs, $\beta \in \{2, 4, 6, 8, 16\}$, while $\gamma \in \{10, 20, 40, 80\}$ for the FVAE were tested on 3D-Shapes and MPI3D, and the model with the smallest loss on the validation set was used for subsequent analysis, which was $\beta = 2$ for the β-VAE and $\beta = 4$ for the β-TCVAE and $\gamma = 40$ for the FVAE. All other method-specific hyperparameters were kept the same in the corresponding papers.

A.3 Additional Results

A.3.1 3D-Shapes

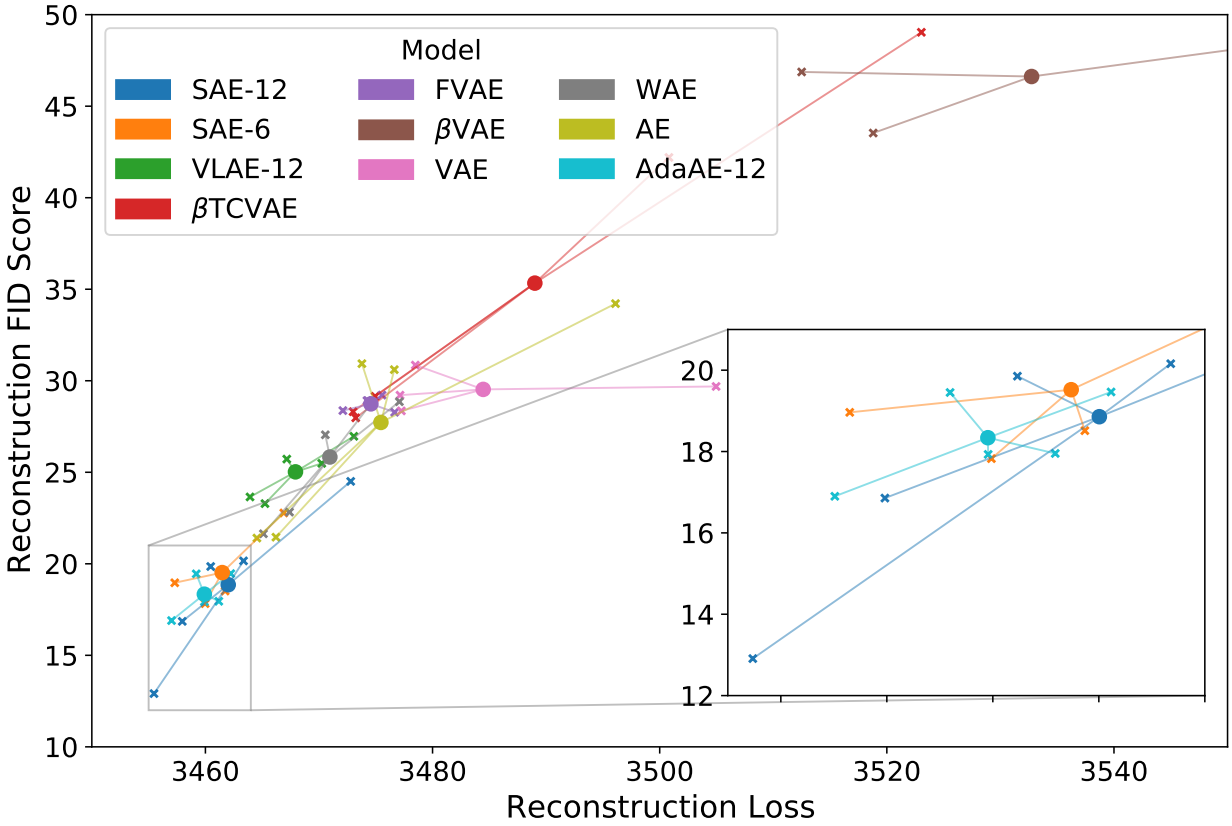

Figure 8: 3D-Shapes reconstruction quality comparison between models using the reconstruction loss (binary cross entropy) and the Fréchet Inception Distance (FID) (Heusel et al., 2017) between the original and reconstructed observations (lower is better for both). Each "x" is a model trained with a unique random seed using the architecture/regularization corresponding to the color. The performance of all the seeds are averaged and plotted as circles "o". Firstly, this plot shows how the reconstruction FID (y-axis) can complement the pixelwise comparison (x-axis) to quantify the quality of the reconstructed samples. Next, the multiple seeds help differentiate the performance of the regularized vs unregularized methods. These regimes separate the models that use the variational regularization loss from the models that only use a reconstruction loss (or a regularization on the aggregated posterior like the WAE). Lastly, the AdaAE-12 slightly out performs the SAE-12 and both of which significantly out perform less structured baselines, which suggests the architectural biases are conducive to high fidelity decoders.

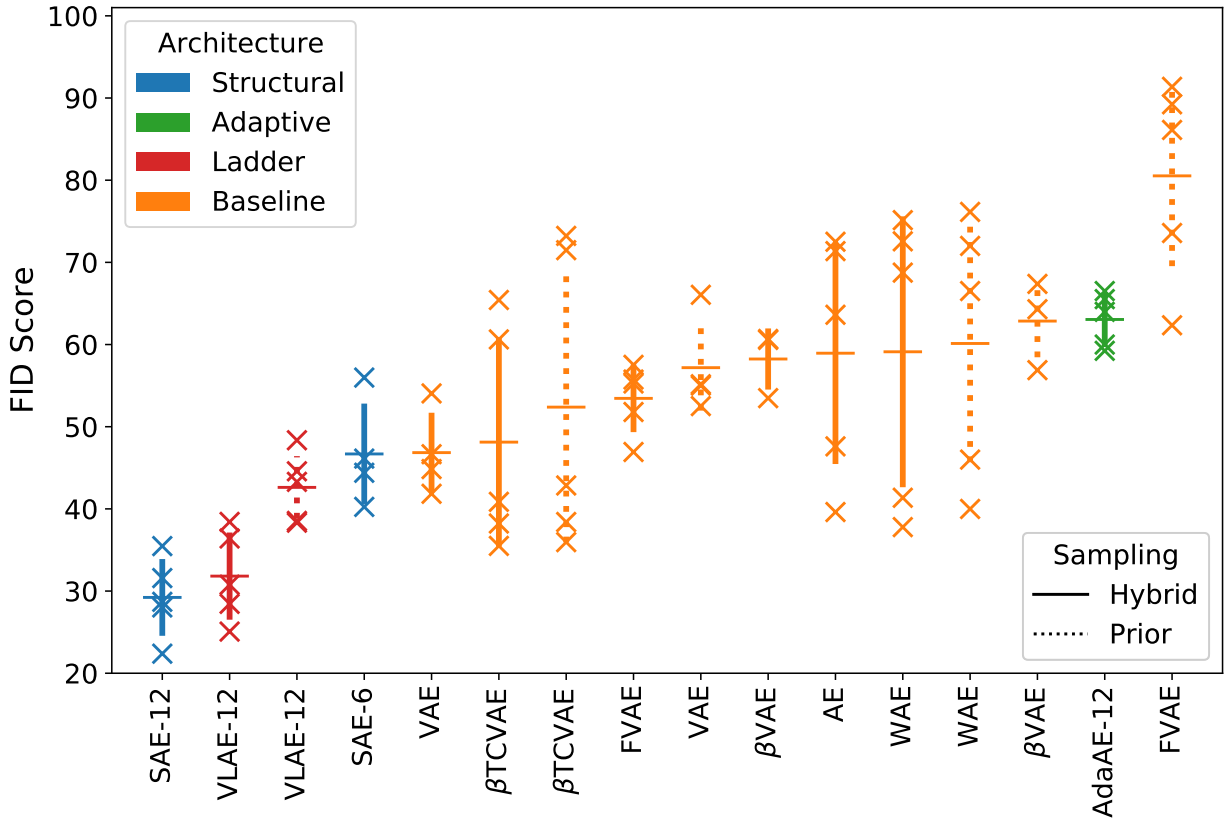

Figure 9: Comparison of the hybrid and prior-based sampling method for all different models. Each "x" corresponds to a unique random seed, the horizontal line corresponds to the mean performance and the vertical line signifies one standard deviation above and below the mean. (lower is best)

Model	DCI	MIG	IRS	Mod	Exp
SAE-12	**0.974**	0.537	**0.830**	**0.967**	**1.000**
SAE-6	0.865	0.225	0.735	0.966	0.999
SAE-4	0.740	0.209	0.654	0.945	0.999
VLAE-12	0.832	**0.553**	0.751	0.914	0.977
VLAE-6	0.785	0.326	0.689	0.929	0.963
VLAE-4	0.690	0.282	0.544	0.900	0.926
βTCVAE	0.410	0.237	0.603	0.865	0.923
FVAE	0.330	0.123	0.725	0.907	0.955
βVAE	0.235	0.127	0.593	0.879	0.799
VAE	0.314	0.138	0.607	0.892	0.872
WAE	0.211	0.050	0.621	0.946	0.906
AE	0.307	0.092	0.638	0.926	0.943
AdaAE-12	0.299	0.062	0.503	0.876	0.999

Table 1: Disentanglement and Completeness scores for 3D-Shapes. The DCI-d metric corresponds to the DCI-disentanglement score and DCI-c to the completeness score (Eastwood & Williams, 2018), IRS is a similar disentanglement metric (Suter et al., 2018), the MIG is the Mutual Information Gap (Chen et al., 2018), and Mod/Exp refers to the Modularity/Explicitness scores respectively (Ridgeway & Mozer, 2018) (for all these metrics higher is better)

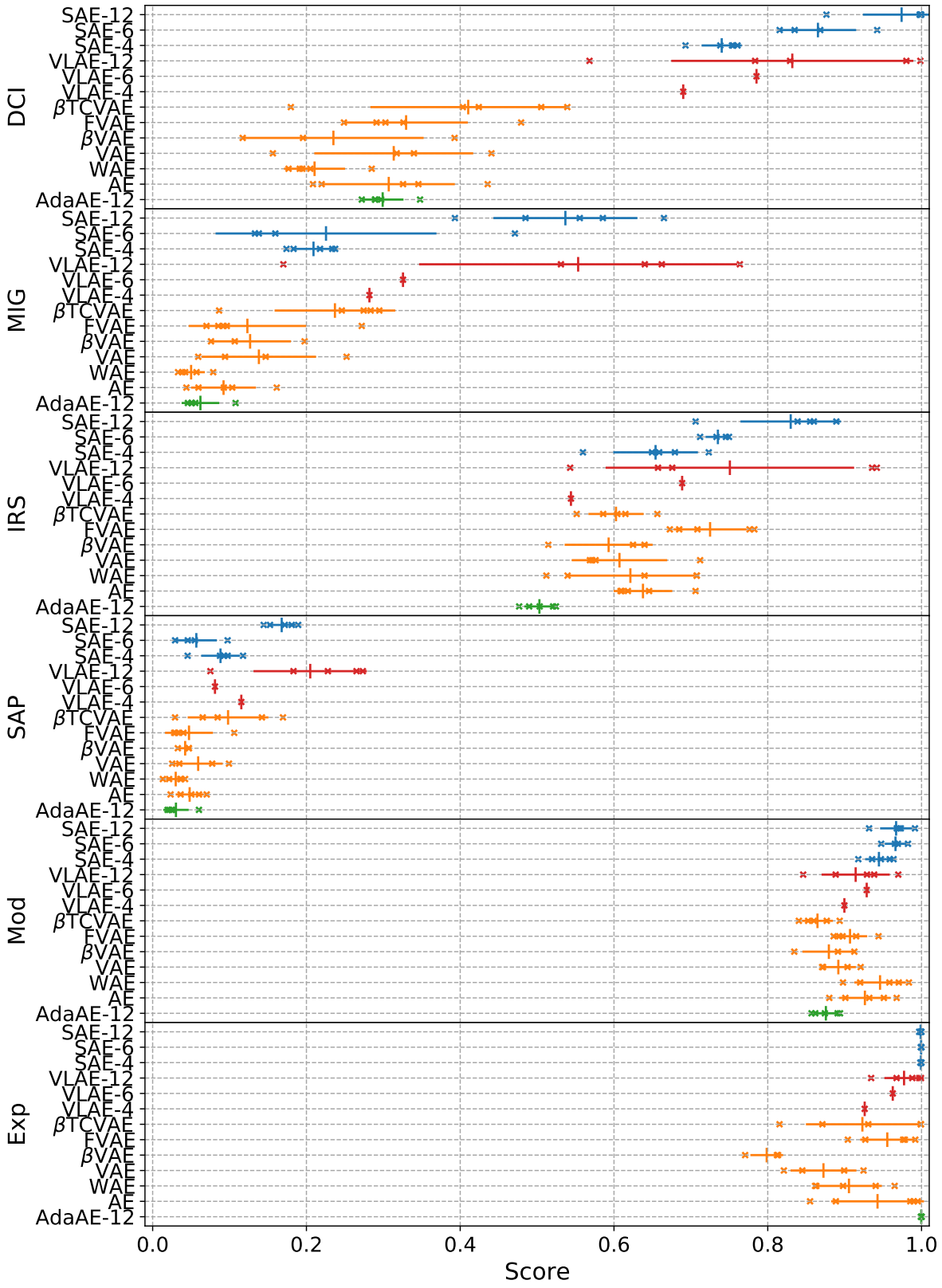

Figure 10: Several disentanglement metrics for all the models and each of the seeds. (for all these metrics higher is better)

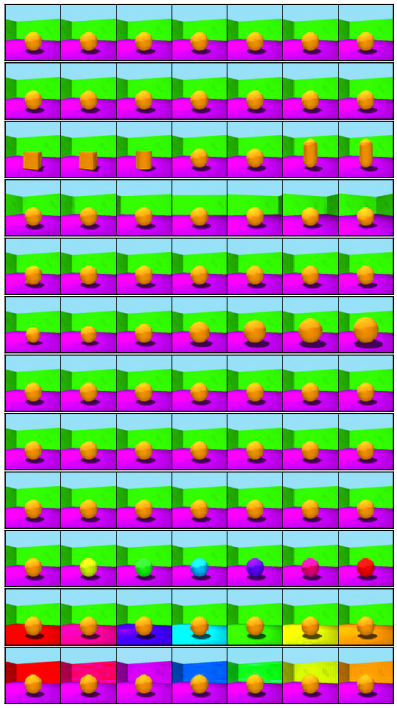

(a) SAE-12

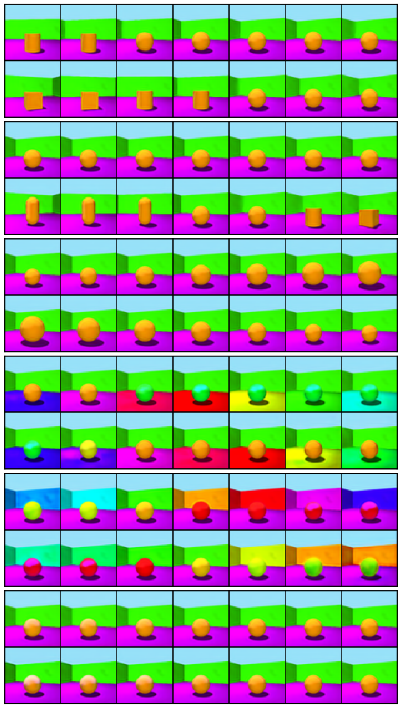

(b) SAE-6

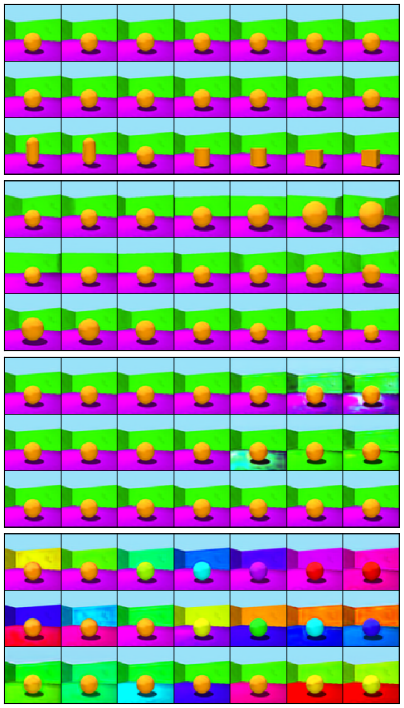

(c) SAE-4

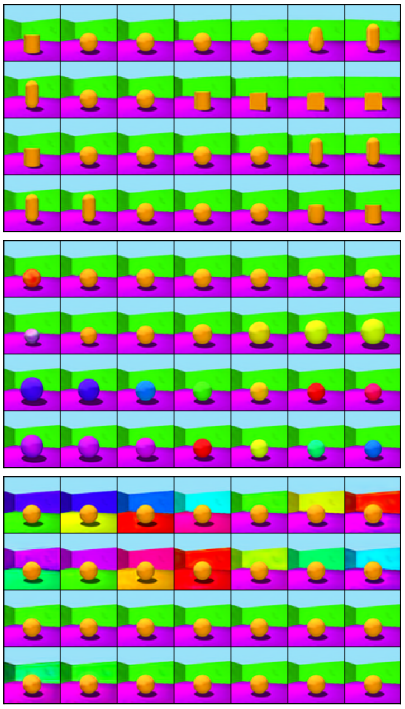

(d) SAE-3

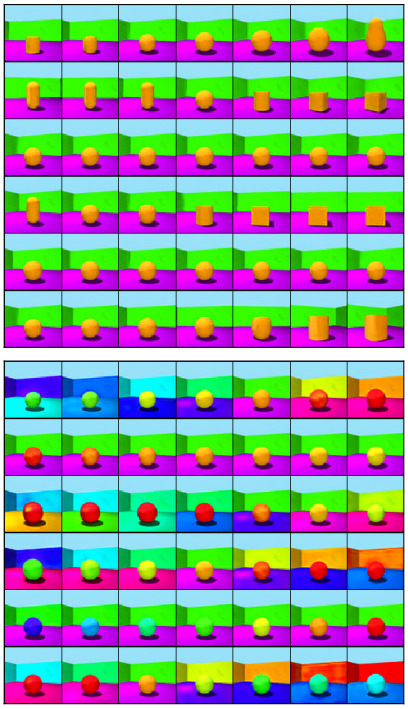

(e) SAE-2

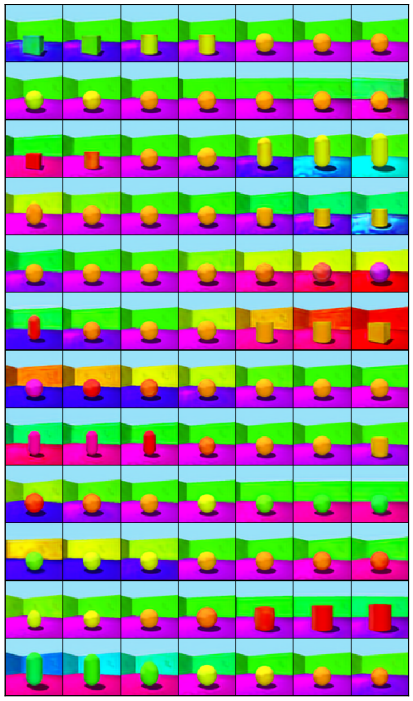

(f) AdaAE-12

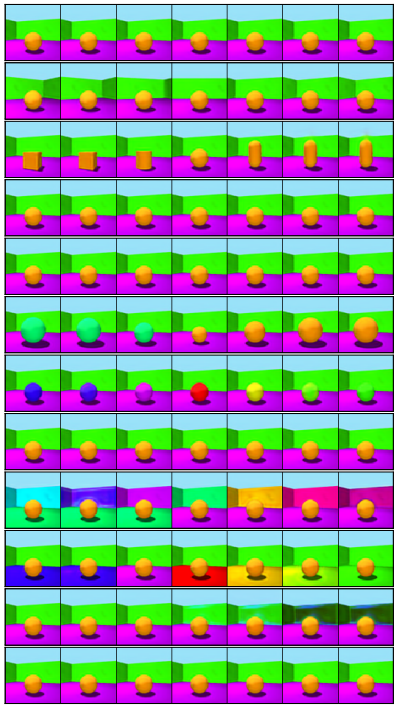

(g) VLAE-12

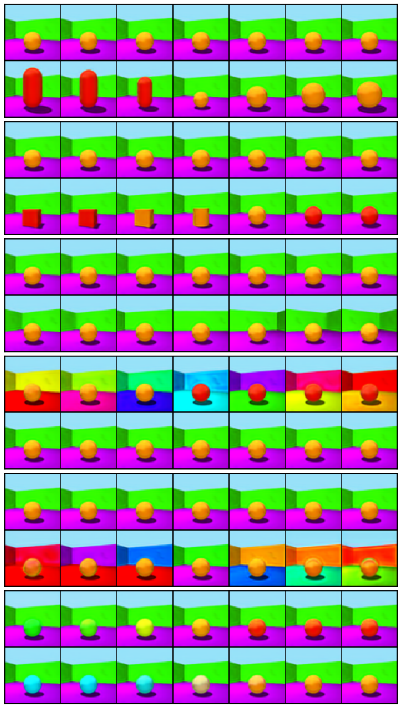

(h) VLAE-6

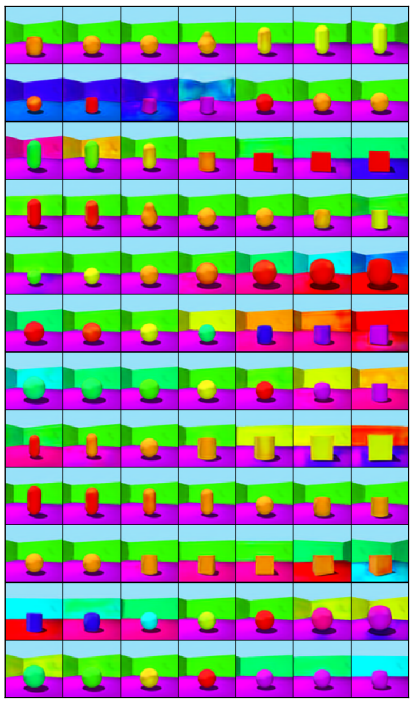

(i) VLAE-4

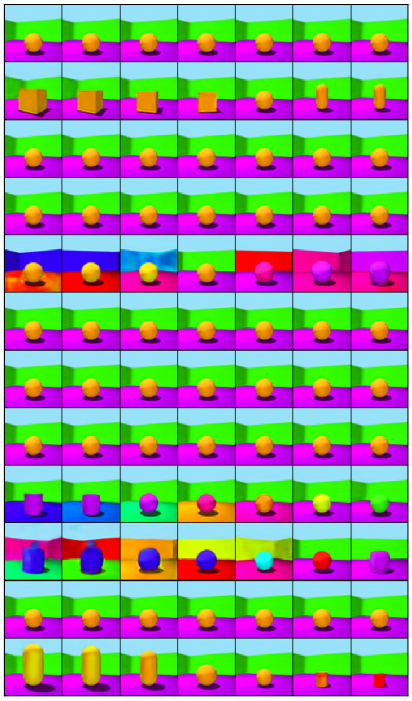

(j) VAE

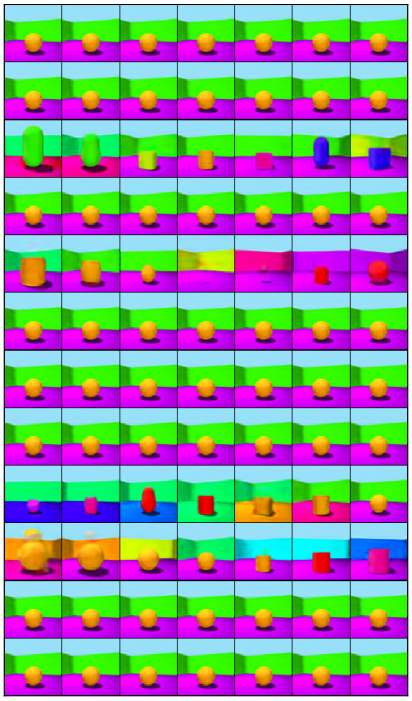

(k) β-VAE

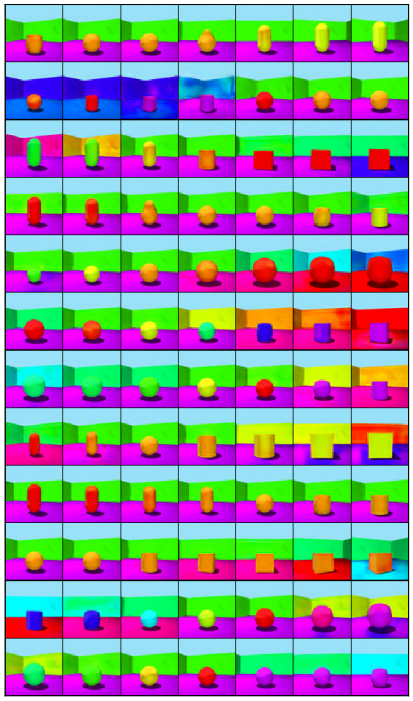

(l) AE

Figure 11: Latent Traversals of several models for 3D-Shapes. Each row shows the generated image when varying the corresponding latent dimension while fixing the rest of the latent vector. For the SAE and VLAE models, the groups of dimensions that are fed into the same Str-Tfm layer (or ladder rung) are grouped together. Note the disentangled segments achieved by the SAE models and the consistent ordering of factors of variation.

A.3.2 Extrapolation

We present results on a variant of the exptrapolation experiment discussed in section 3.2. Instead of modifying the shape in the initial training dataset, we remove the two most extreme camera angles in either direction (removing 4/15 of the full dataset).

As seen from figure 12, in this setting the warping and generally lower fidelity experienced by only updating the encoder compared to updating the decoder is very apparent.

Model	Neither	Encoder	Decoder	Both
SAE-12	4.88	**2.65**	0.77	0.43
VLAE-12	6.91	3.83	1.61	0.77
AdaAE-12	4.8	2.93	**0.59**	**0.41**
AE	4.98	2.94	0.62	0.45
WAE	**4.79**	3.07	0.69	0.44
VAE	5.17	3.09	1.01	0.51
βVAE	5.7	3.97	1.5	0.82

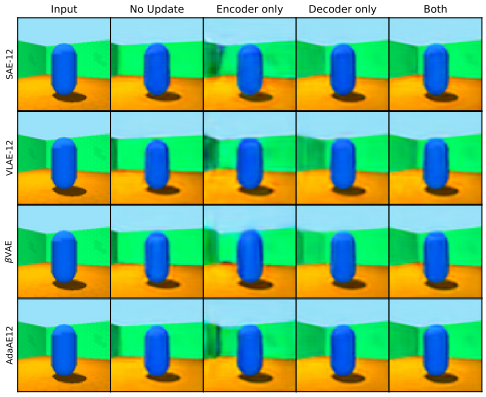

Figure 12: Same as figure 7, except for the camera angle setting. Although the results are generally very consistent, note how much better the SAE-12 model performs than the VLAE-12 in this setting.

A.3.3 MPI3D-Toy

Model	DCI	MIG	IRS	Mod	Exp
SAE-12	**0.642**	**0.487**	0.570	0.938	**0.946**
SAE-6	0.454	0.094	0.553	0.918	0.911
VLAE-12	0.414	0.323	0.667	0.909	0.842
βTCVAE	0.091	0.007	0.605	0.858	0.678
FVAE	0.108	0.029	0.680	0.876	0.743
βVAE	0.046	0.004	**0.987**	**0.998**	0.621
VAE	0.093	0.078	0.621	0.861	0.659
WAE	0.203	0.028	0.633	0.904	0.859
AE	0.186	0.043	0.632	0.911	0.844
AdaAE-12	0.208	0.080	0.546	0.919	0.931

Table 2: Disentanglement and Completeness scores for MPI3D-Toy. (for all these metrics higher is better)

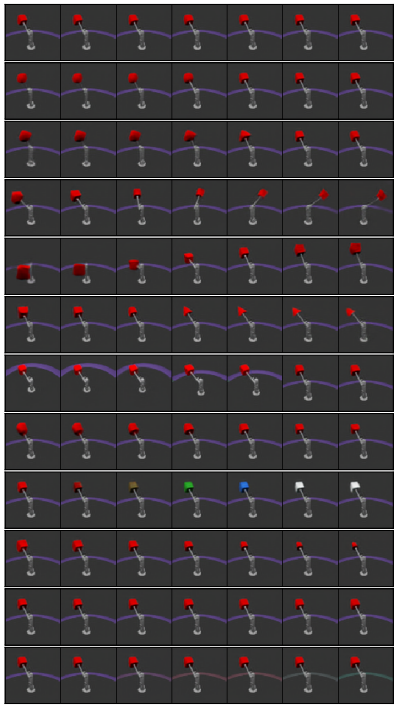

(a) SAE-12

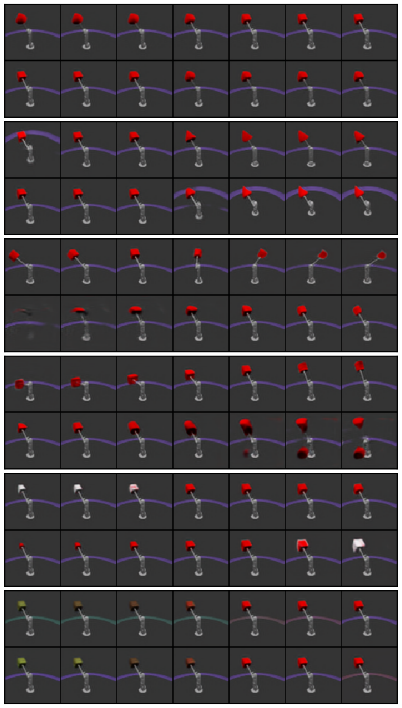

(b) SAE-6

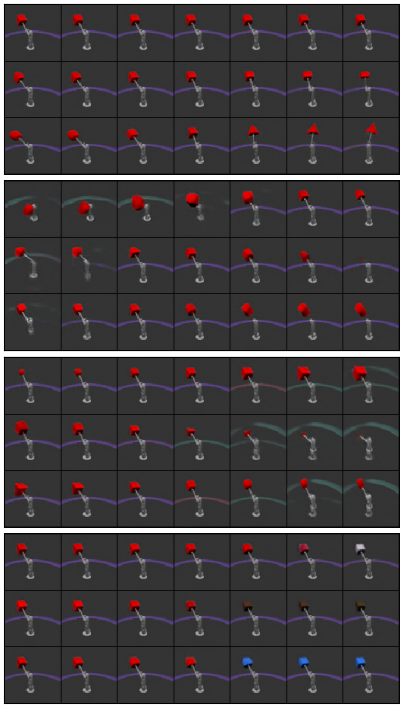

(c) SAE-4

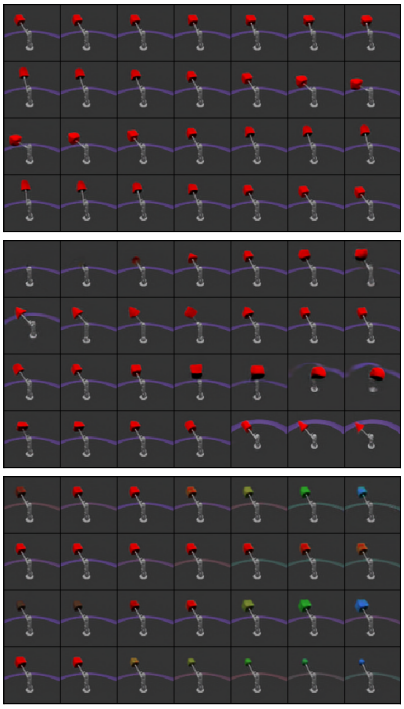

(d) SAE-3

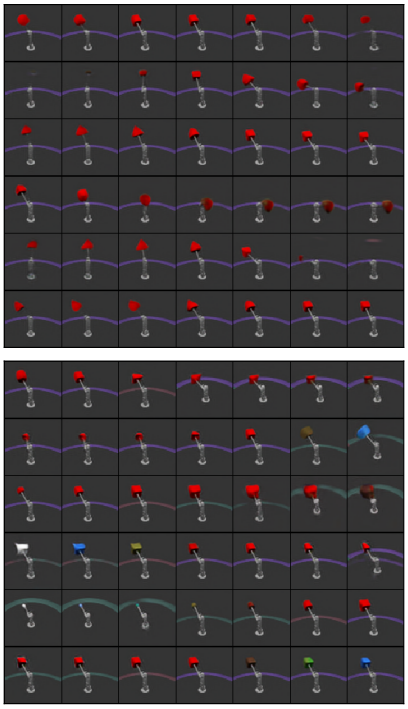

(e) SAE-2

(f) AdaAE-12

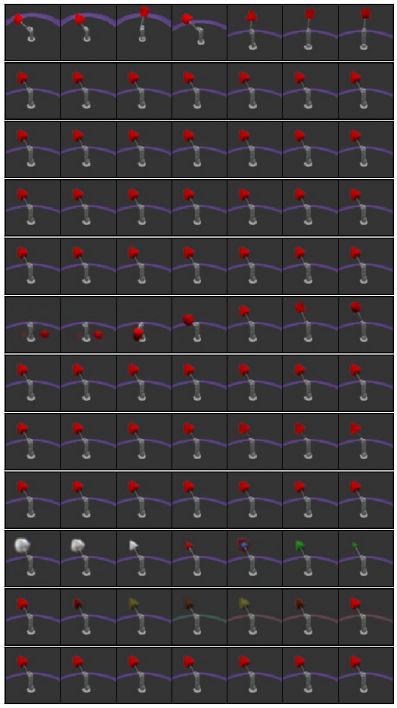

(g) VLAE-12

(h) VLAE-6

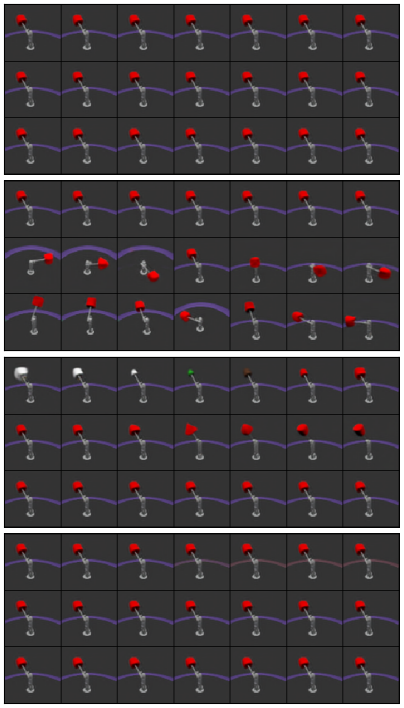

(i) VLAE-4

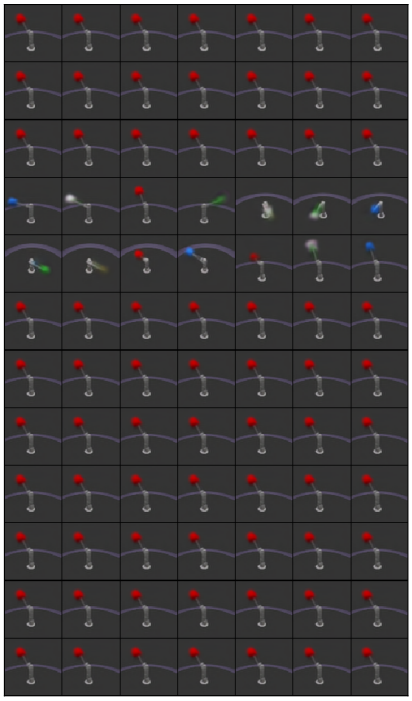

(j) VAE

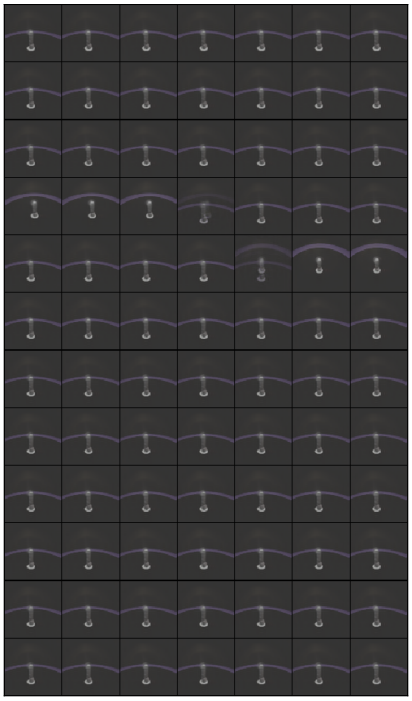

(k) β-VAE

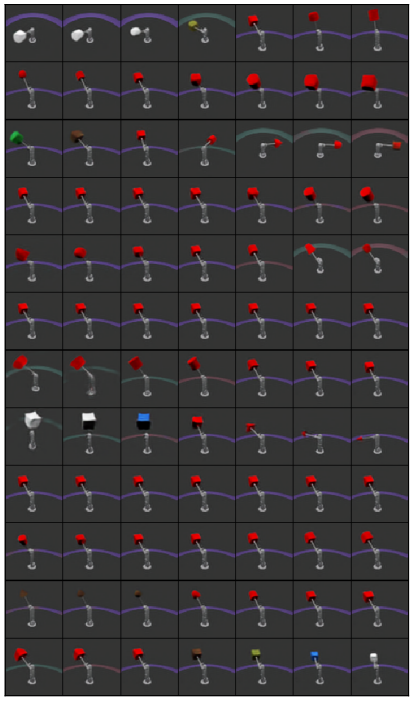

(l) AE

Figure 13: Latent Traversals of several models for MPI3D-Toy. Each row shows the generated image when varying the corresponding latent dimension while fixing the rest of the latent vector. For the SAE and VLAE models, the groups of dimensions that are fed into the same Str-Tfm layer (or ladder rung) are grouped together. Note the disentangled segments achieved by the SAE models and the consistent ordering of factors of variation.

A.3.4 MPI3D-Sim

Model	DCI	MIG	IRS	Mod	Exp
SAE-12	**0.411**	**0.238**	0.508	**0.930**	0.890
SAE-6	0.294	0.052	0.479	0.928	0.877
VLAE-12	0.220	0.093	0.634	0.863	0.816
βTCVAE	0.148	0.139	0.688	0.856	0.694
FVAE	0.095	0.044	0.664	0.916	0.722
βVAE	0.060	0.054	**0.850**	0.926	0.701
VAE	0.070	0.056	0.850	0.828	0.713
WAE	0.129	0.033	0.548	0.881	0.819
AE	0.157	0.033	0.526	0.855	0.805
AdaAE-12	0.159	0.022	0.481	0.893	**0.905**

Table 3: Disentanglement and Completeness scores for MPI3D-Sim. (for all these metrics higher is better)

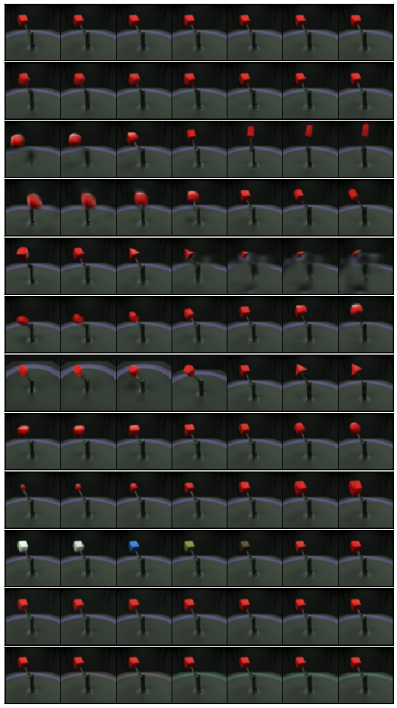

(a) SAE-12

(b) SAE-6

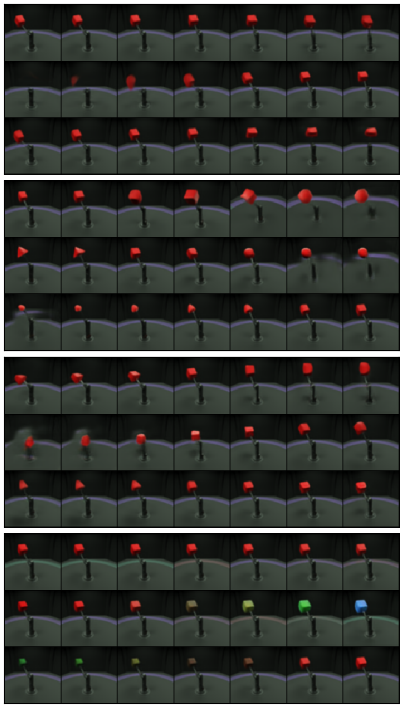

(c) SAE-4

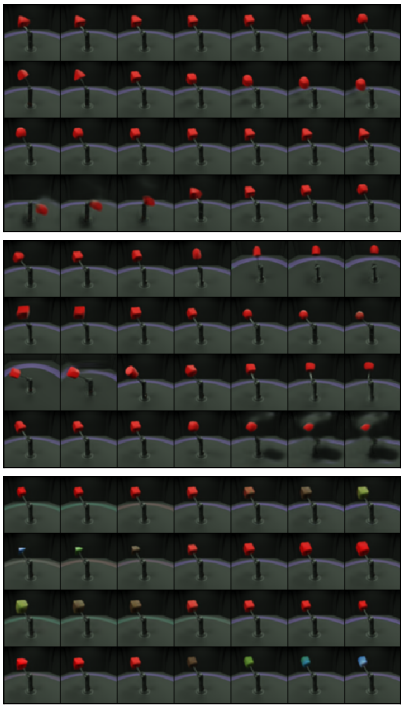

(d) SAE-3

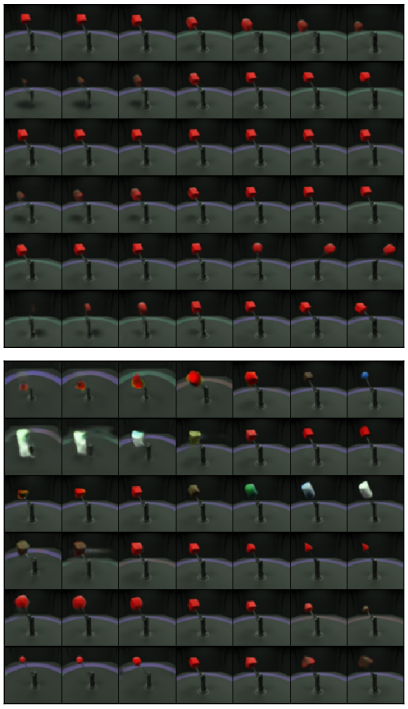

(e) SAE-2

(f) AdaAE-12

(g) VLAE-12

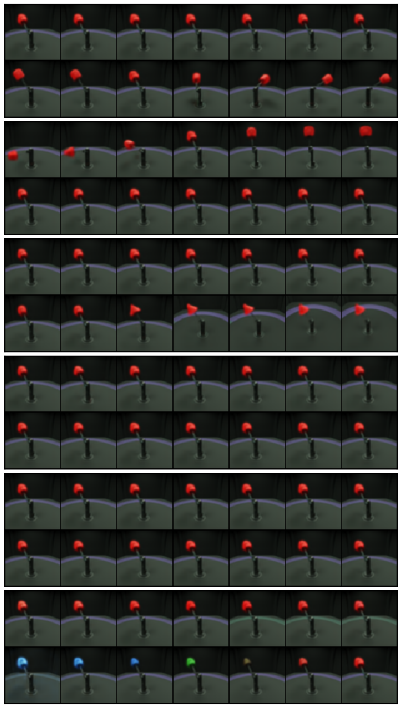

(h) VLAE-6

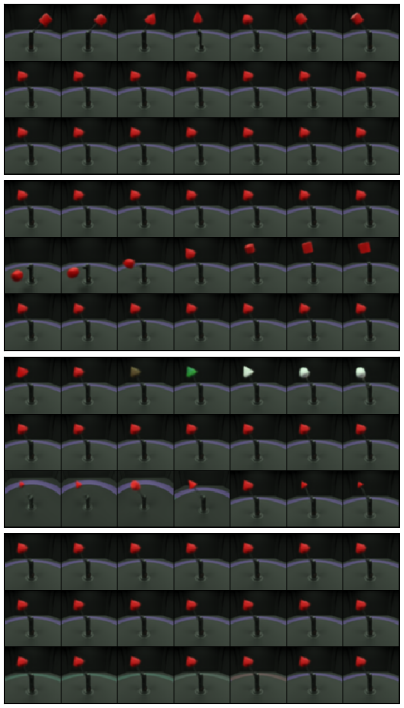

(i) VLAE-4

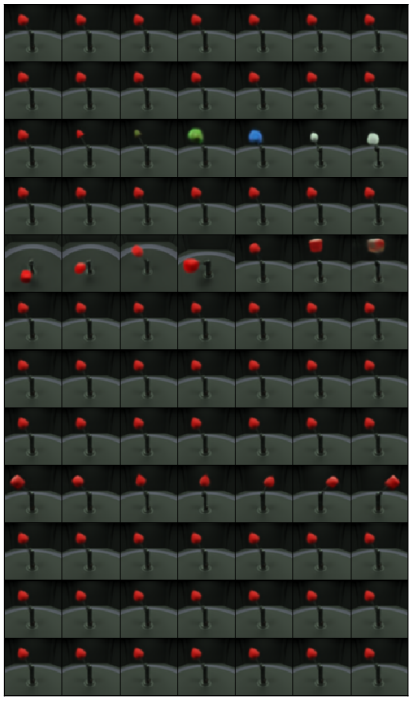

(j) VAE

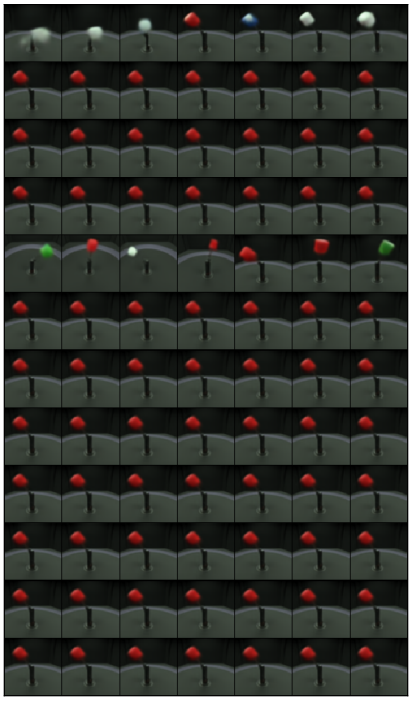

(k) β-VAE

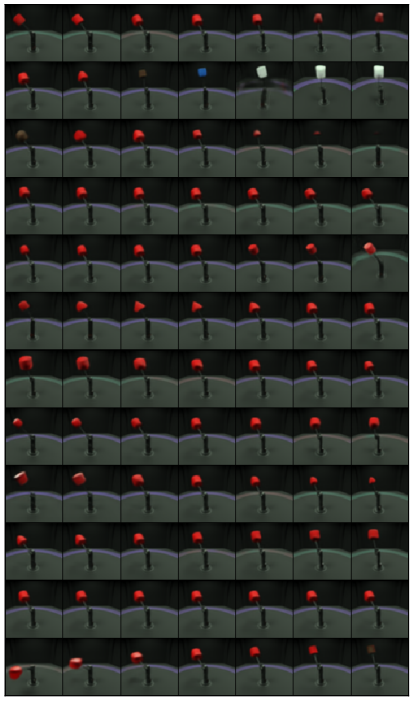

(l) AE

Figure 14: Latent Traversals of several models for MPI3D-Sim. Each row shows the generated image when varying the corresponding latent dimension while fixing the rest of the latent vector. For the SAE and VLAE models, the groups of dimensions that are fed into the same Str-Tfm layer (or ladder rung) are grouped together. Note the disentangled segments achieved by the SAE models and the consistent ordering of factors of variation.

A.3.5 MPI3D-Real

Model	DCI	MIG	IRS	Mod	Exp
SAE-12	**0.374**	0.148	0.564	0.928	0.869
SAE-6	0.295	0.074	0.535	0.879	0.840
VLAE-12	0.291	**0.217**	0.579	0.914	0.805
βTCVAE	0.185	0.100	0.595	0.870	0.699
FVAE	0.095	0.028	0.522	0.904	0.729
βVAE	0.090	0.021	**0.659**	0.869	0.680
VAE	0.080	0.020	0.602	0.875	0.694
WAE	0.159	0.042	0.587	0.837	0.831
AE	0.143	0.048	0.563	0.858	0.804
AdaAE-12	0.164	0.034	0.530	**0.952**	**0.895**

Table 4: Disentanglement and Completeness scores for MPI3D-Real. (for all these metrics higher is better)

(a) SAE-12

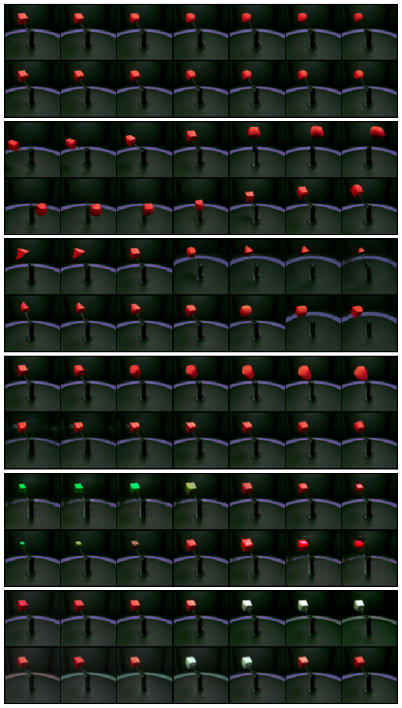

(b) SAE-6

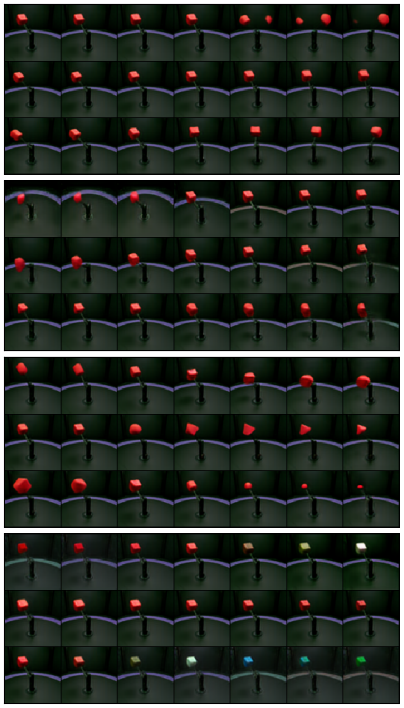

(c) SAE-4

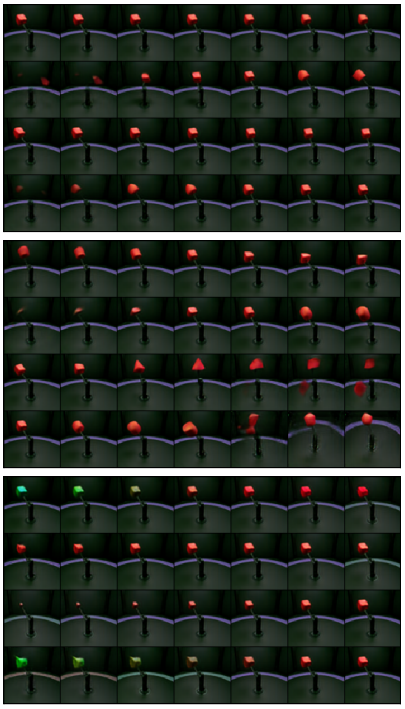

(d) SAE-3

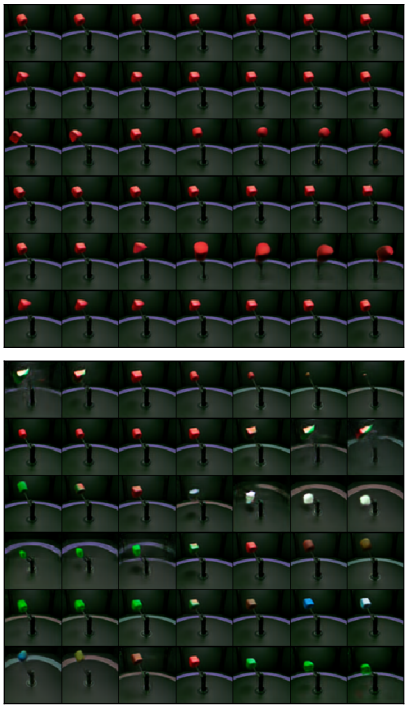

(e) SAE-2

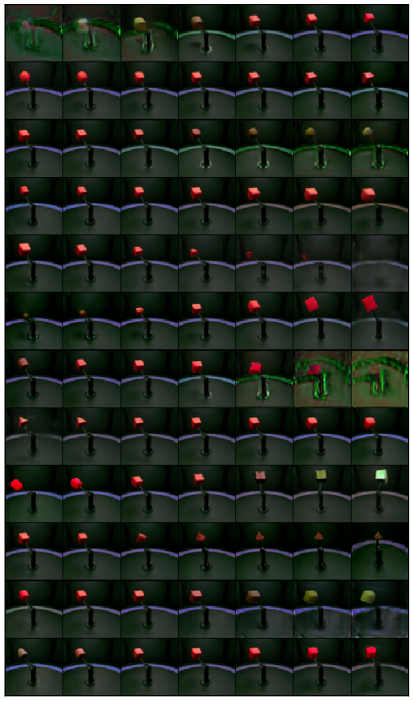

(f) AdaAE-12

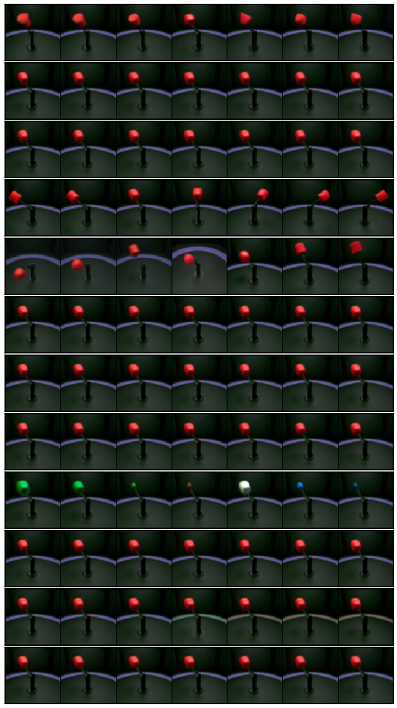

(g) VLAE-12

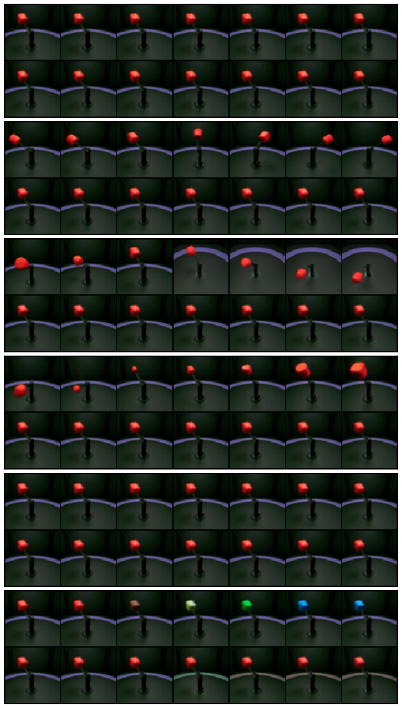

(h) VLAE-6

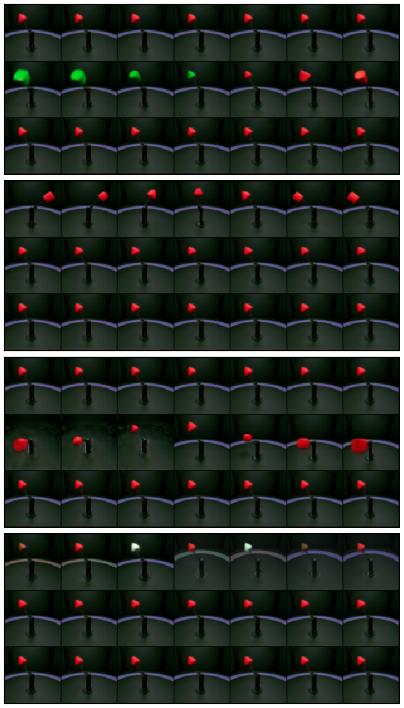

(i) VLAE-4

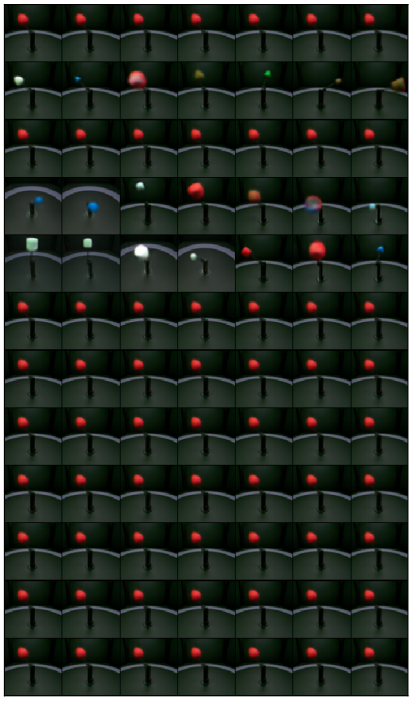

(j) VAE

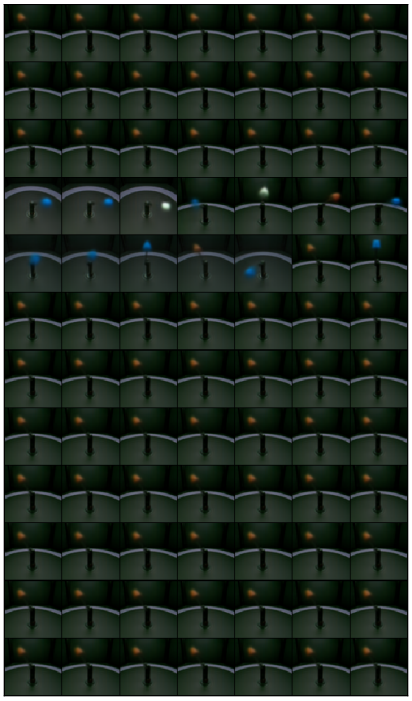

(k) β-VAE

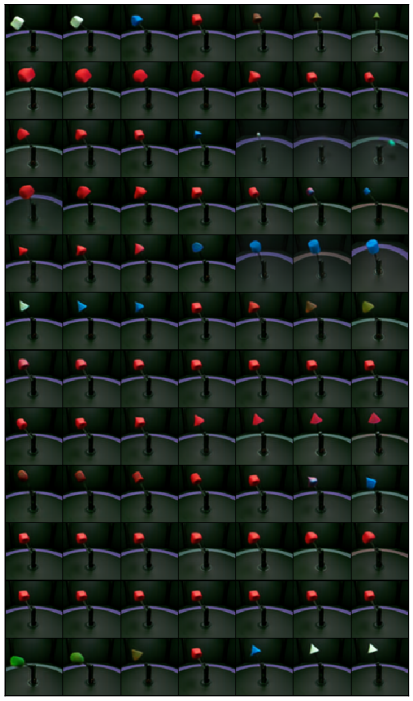

(l) AE

Figure 15: Latent Traversals of several models for MPI3D-Real. Each row shows the generated image when varying the corresponding latent dimension while fixing the rest of the latent vector. For the SAE and VLAE models, the groups of dimensions that are fed into the same Str-Tfm layer (or ladder rung) are grouped together. Note the disentangled segments achieved by the SAE models and the consistent ordering of factors of variation.

A.3.6 Celeb-A

(a) Original samples (from test set)

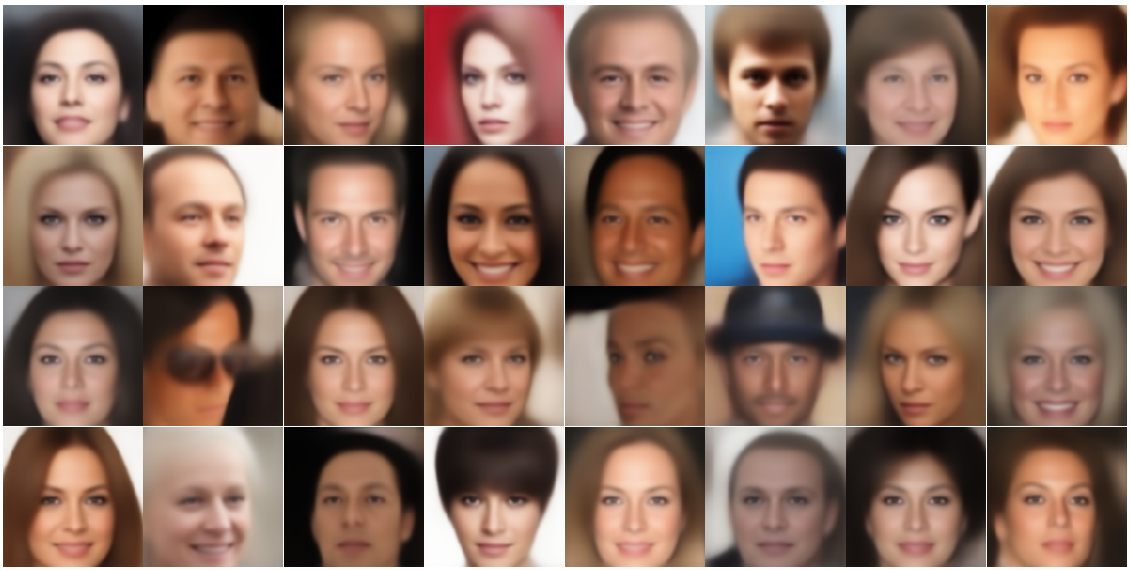

(b) SAE-16 Reconstructions

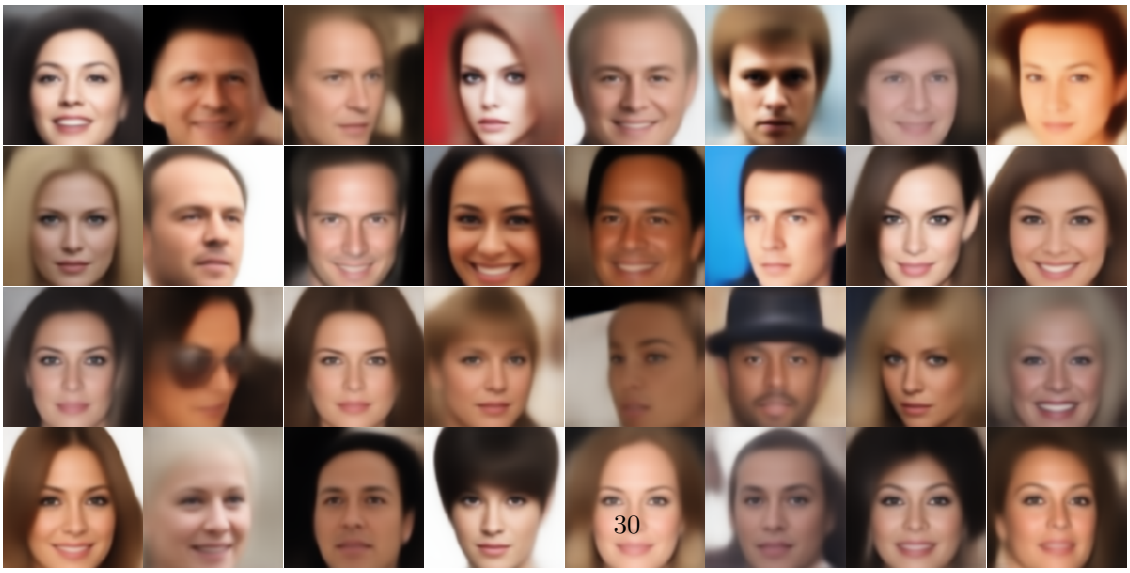

(c) AdaAE-16 Reconstructions

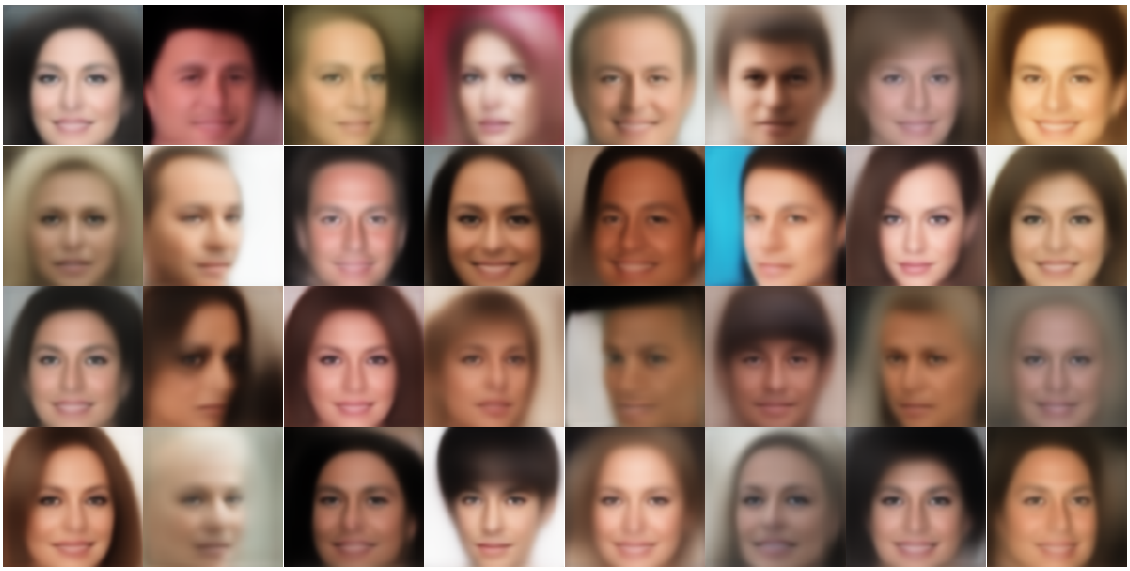

(d) VLAE-16 Reconstructions

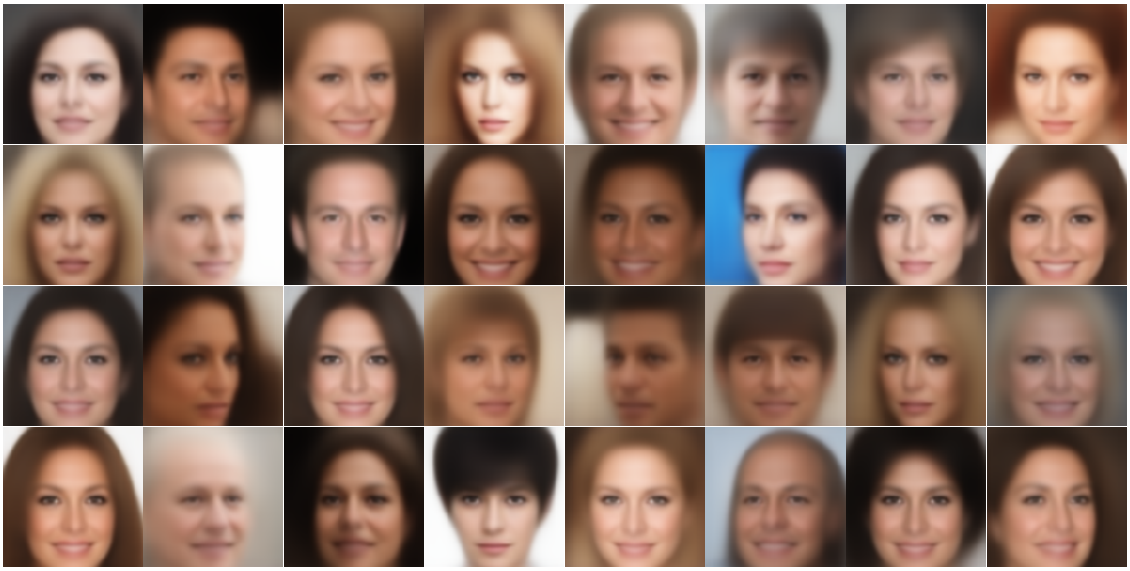

(e) VAE Reconstructions

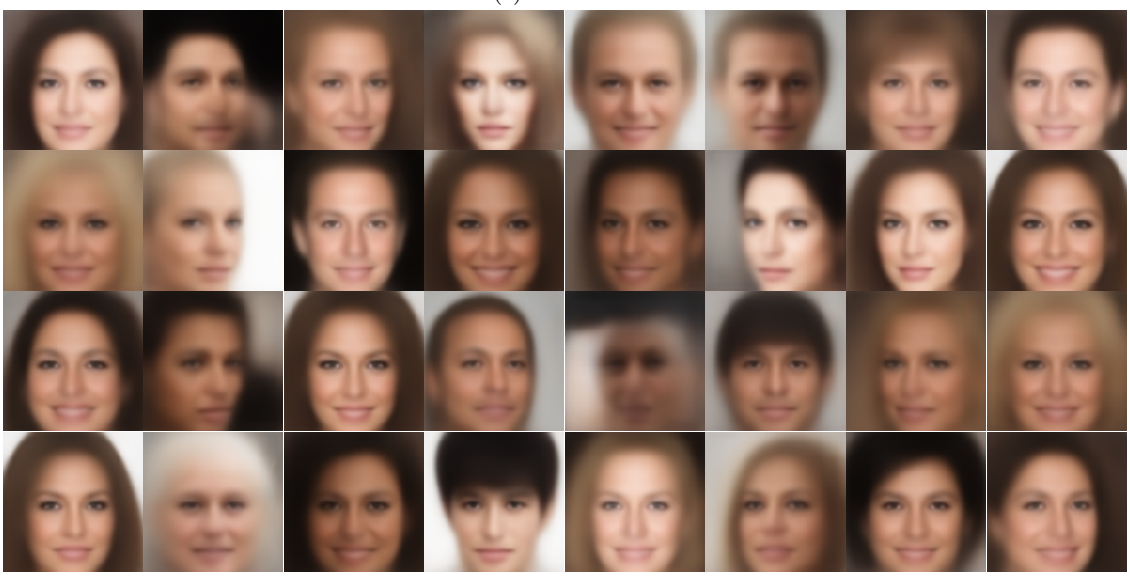

(f) AE Reconstructions

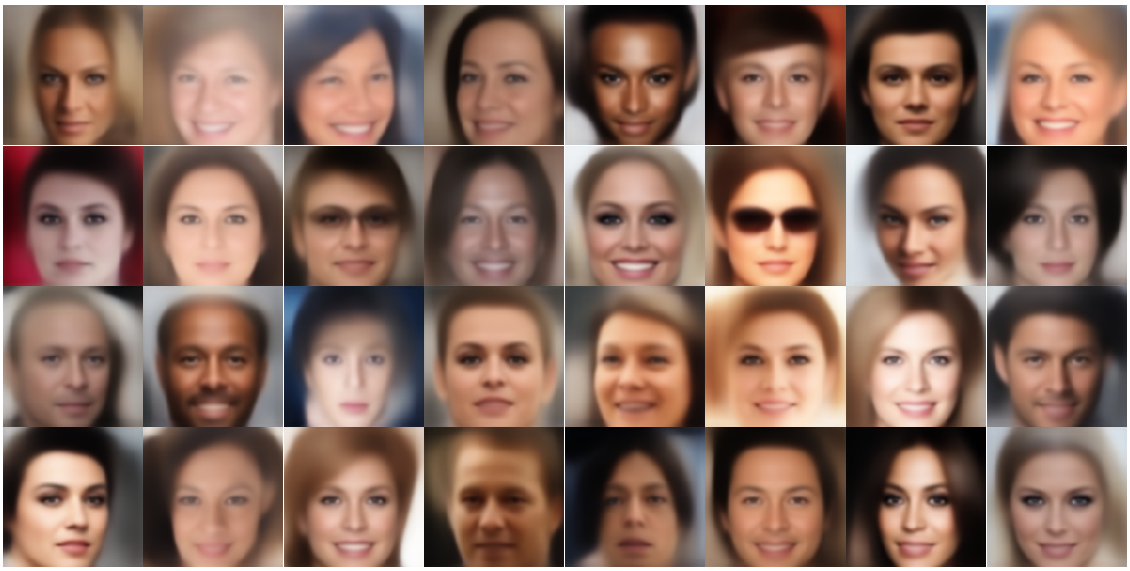

(a) SAE-16 Hybrid Sampling

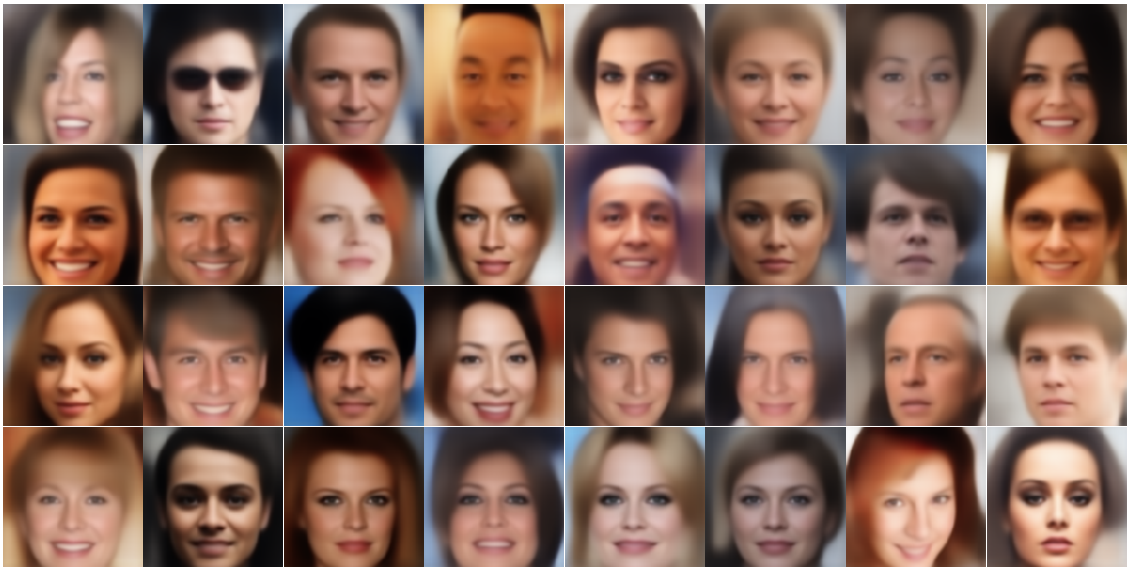

(b) AdaAE-16 Hybrid Sampling

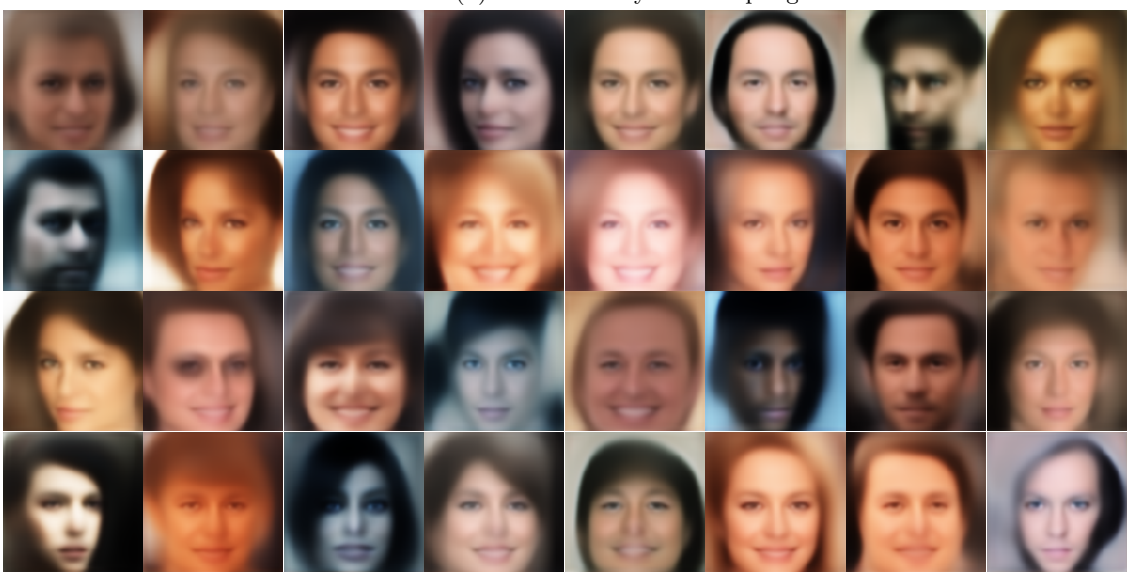

(c) VLAE-16 Hybrid Sampling

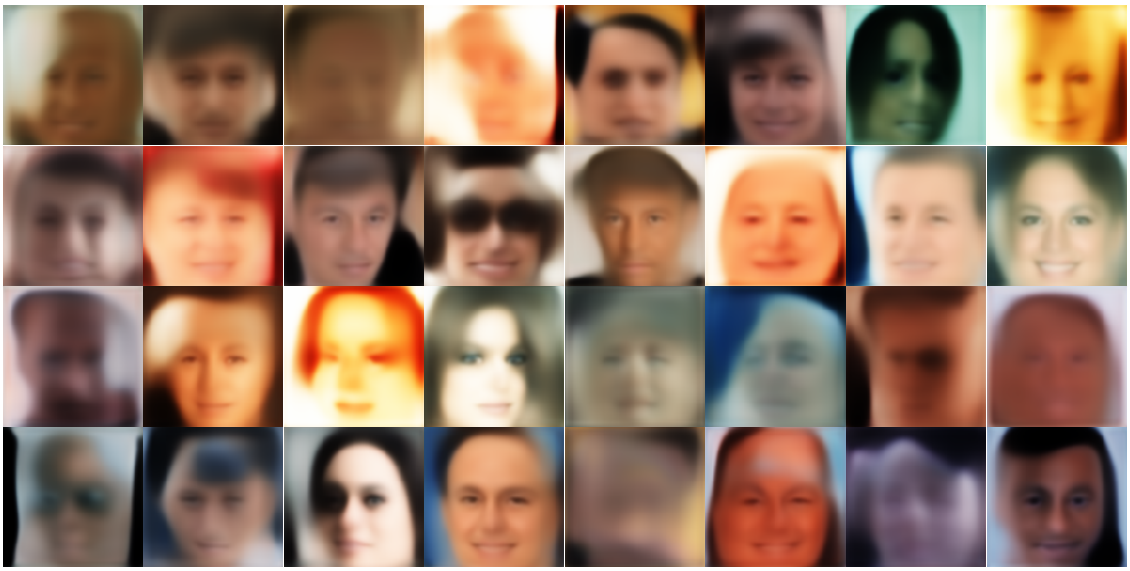

(d) VLAE-16 Prior Sampling

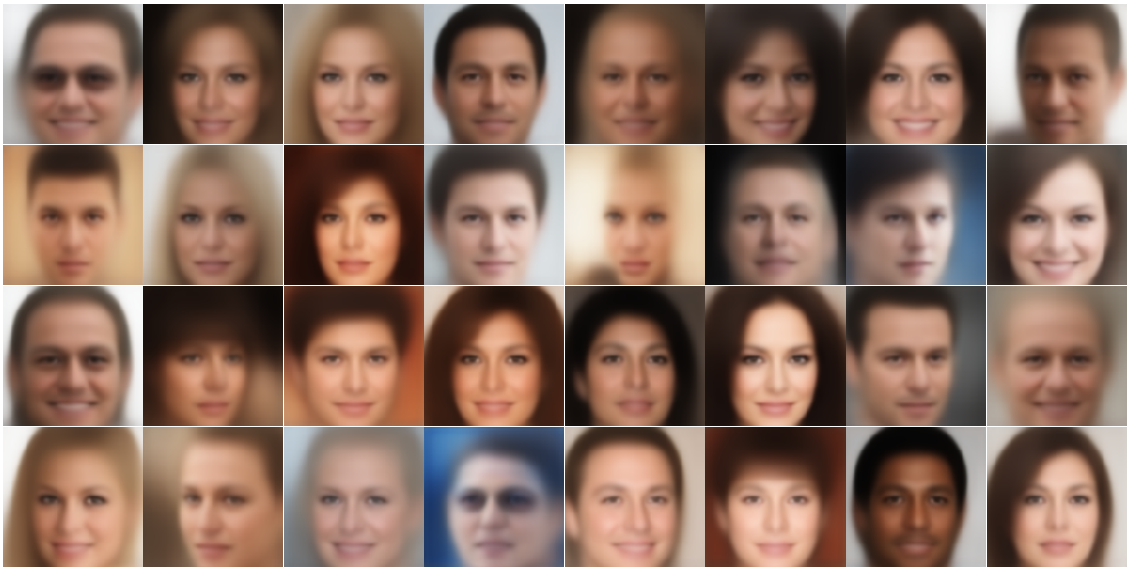

(e) VAE Hybrid Sampling

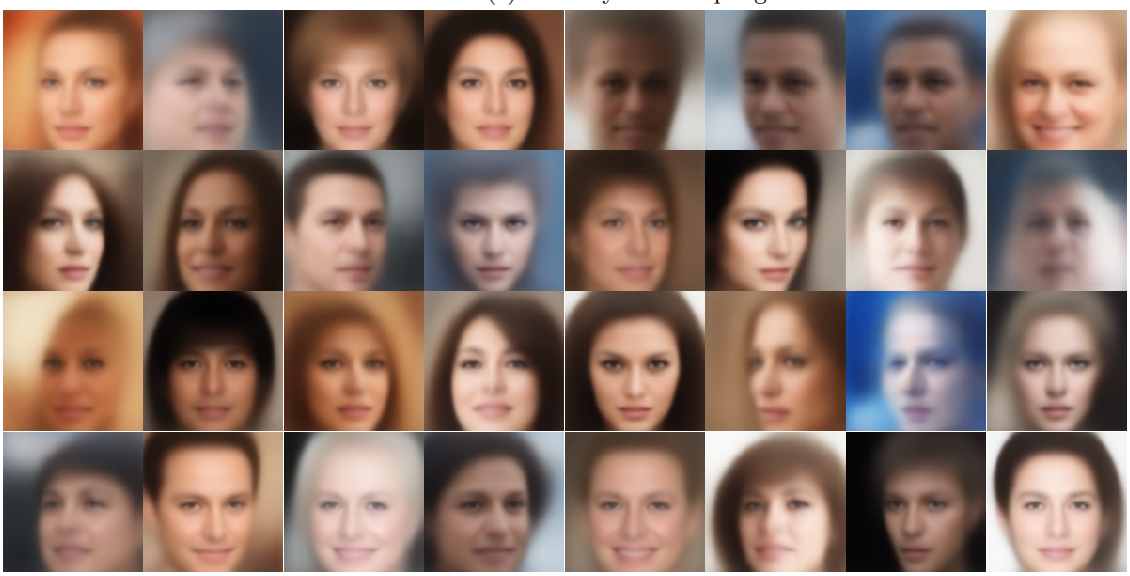

(f) VAE Prior Sampling

A.3.7 RFD

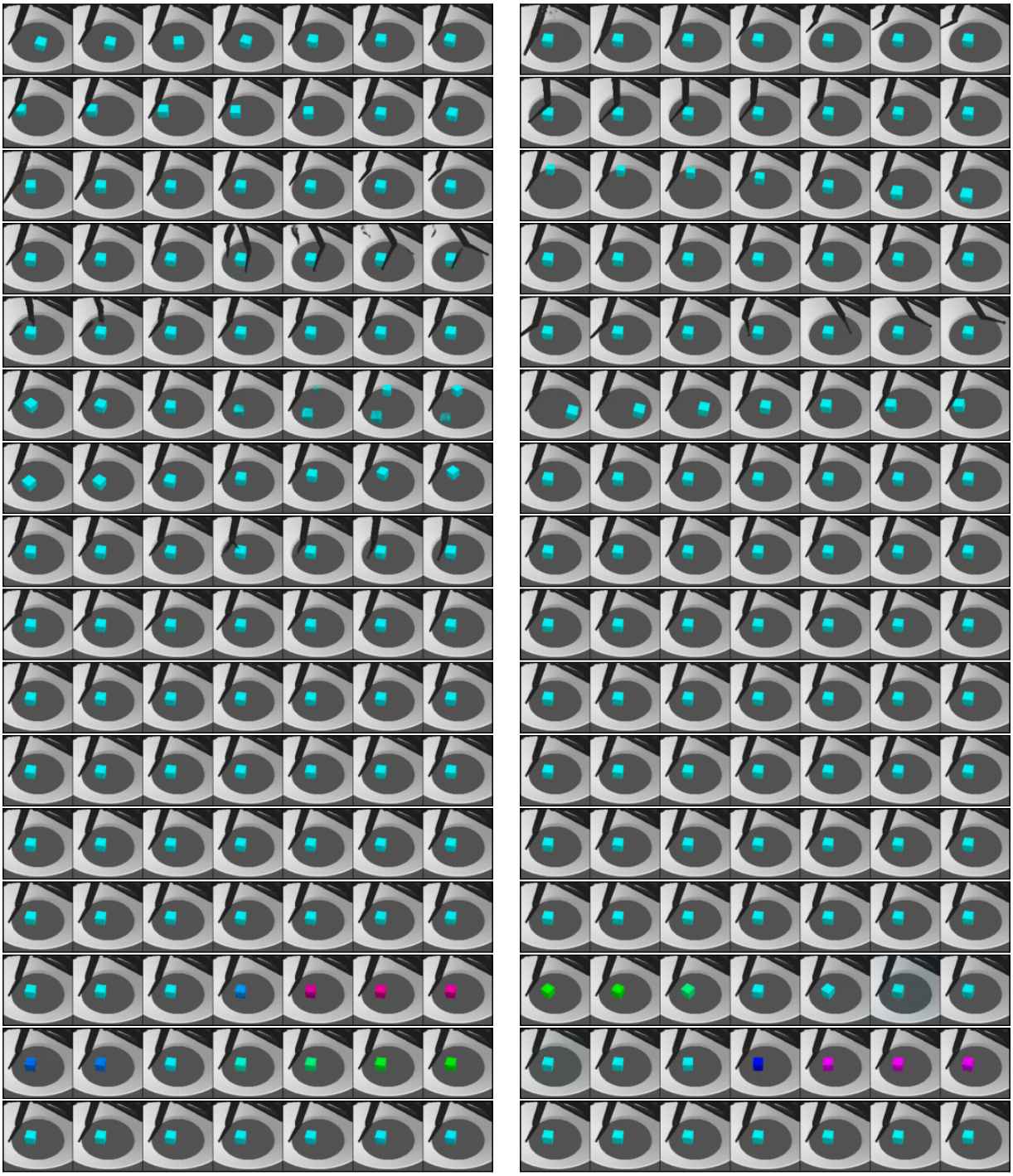

(a) SAE-16

(b) VLAE-16

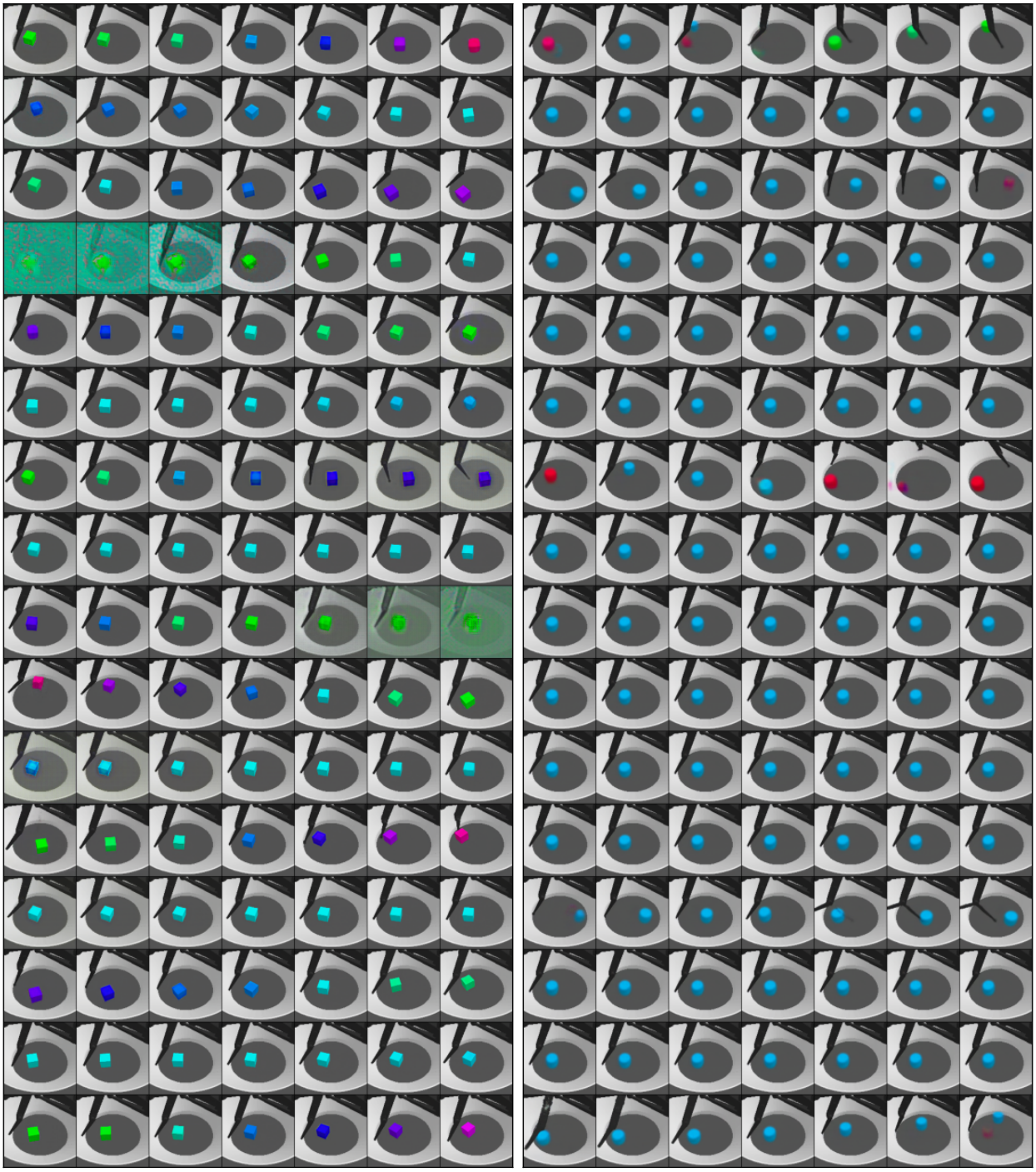

(c) AdaAE-16 (d) VAE

Figure 18: Latent traversals for the RFD dataset. Each row corresponds to a 1D traversal of the corresponding latent dimension while the other latent dimensions are fixed. Note the ordering of information in the more structured models like the SAE-16 and VLAE-16.